Is the Brightest Galaxy behind the Bullet Cluster a Galaxy in the Making?

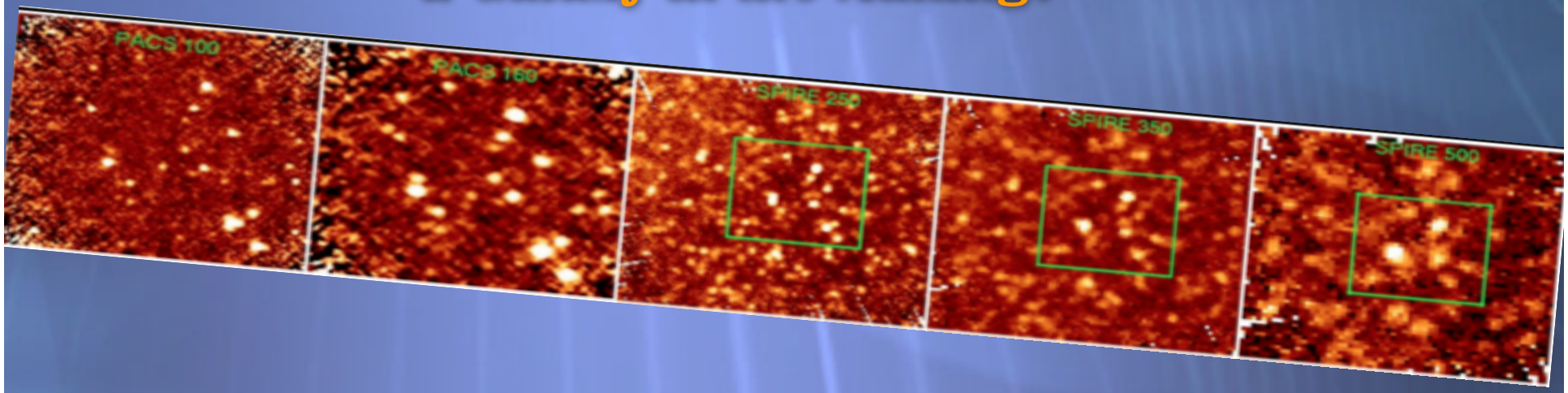

Omar López-Cruz*

Coordinación de Astrofísca, Instituto Nacional de Astrofísica, Optica y Electrónica (INAOE)

omarlx@inaoep.mx

*Visiting Scientist, Astrophysics Group, Bristol

The Team

- Mark Birkinshaw, Malcolm Bremer, Kathy Lancaster at Bristol University, UK
- Frank Bertoldi, K. Basu, M.W. Sommer & Padeli Papadopoulos at Argelander-Institute für Astronomie, Germany
- Kathy Horellou, Daniel Johansson (PhD 2011), Sebastian Muller, and John H. Black at Chalmers University of Technology, Sweden
- Omar López-Cruz, Olga Vega, W. F. Wall, Héctor J. Ibarra-Medel and Edgar Castillo-Dominguez at INAOE
- Hernán Quintana at PUC, Chile

Science

- The results to be presented in this talk come from three publications:

- Johansson, D., Horellou, C., Sommer, M.~W., et al. 2010, A&A, 514, A77

- Johansson, D., Horellou, C., López-Cruz, et al, 2012, to be published in A&A

- López-Cruz et al. 2012 (in preparation)


The Bullet Cluster (1E 0657 -57) was discovered by Tucker et al. (1995) using *Einstein IPC*. Tucker et al. (1998) used ASCA data and derived T= 17 keV (5.2 X 10^8 K), one of the hottest known cluster. Established as a cluster-cluster merger by Tucker et al. (1998a) using ROSAT. The most luminous synchrotron radio halo (Liang et al. 2000). Supersonic merger Mach=2-3 shock: v=4000-5000 km/s (Markevitch et al. 2002)

Physical Properties of the gas in the Bullet Cluster (Markevitch et al. ,2002)

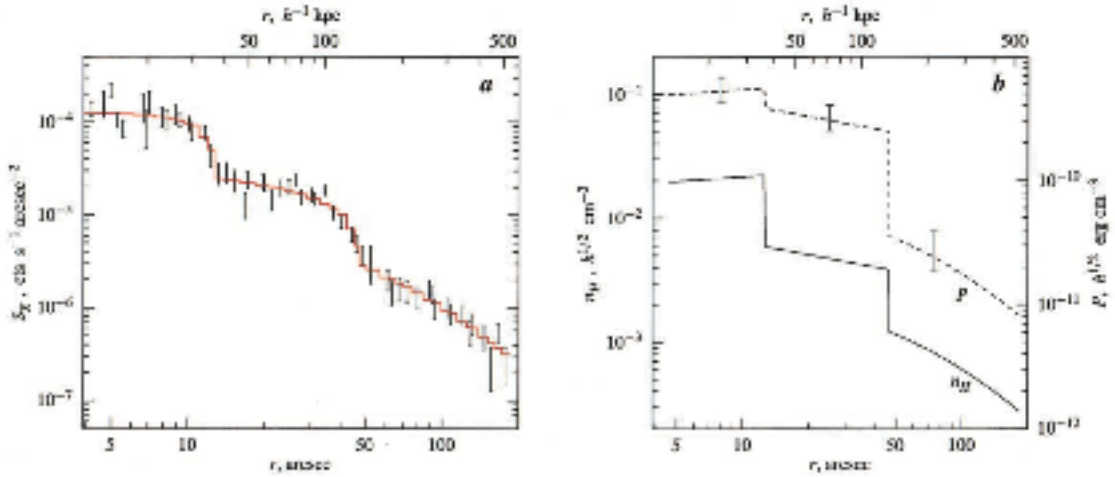

FIG. 4.—(*a*) ACIS 0.5–5 keV surface brightness profile in a 120° sector centered on the bullet and directed westward. The profile is extracted in elliptical segments parallel to the shock front; the *r*-coordinate corresponds to an average radius within a segment. Errors in this figure are 1 σ. The histogram shows the best-fit model (see text). The corresponding unprojected model density profile along the symmetry axis is shown in (*b*), which also includes an approximate gas pressure model using temperatures in regions B, S, and P from Fig. 2. Error bars on pressure correspond to errors in temperature.

LIANG ET AL. Vol. 544

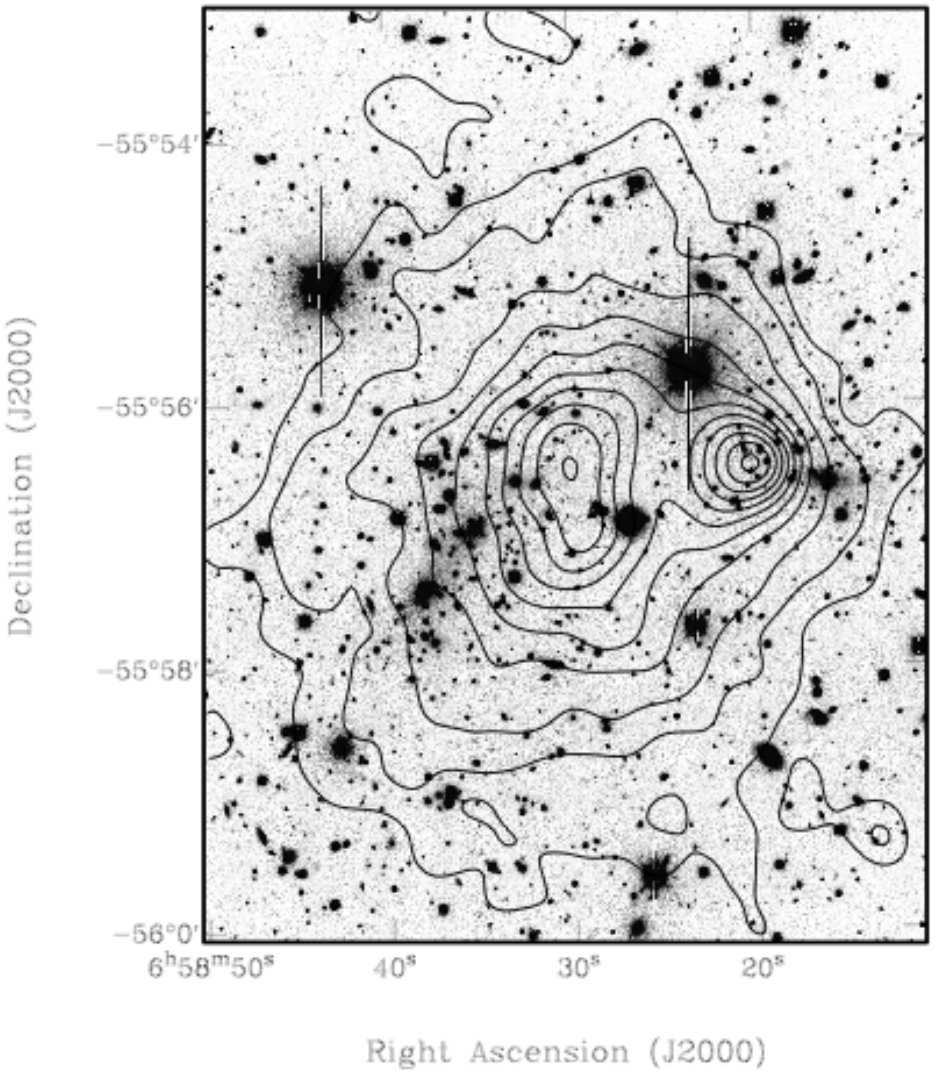

Liang et al. (2000)
1.3 GHz ATCA observations

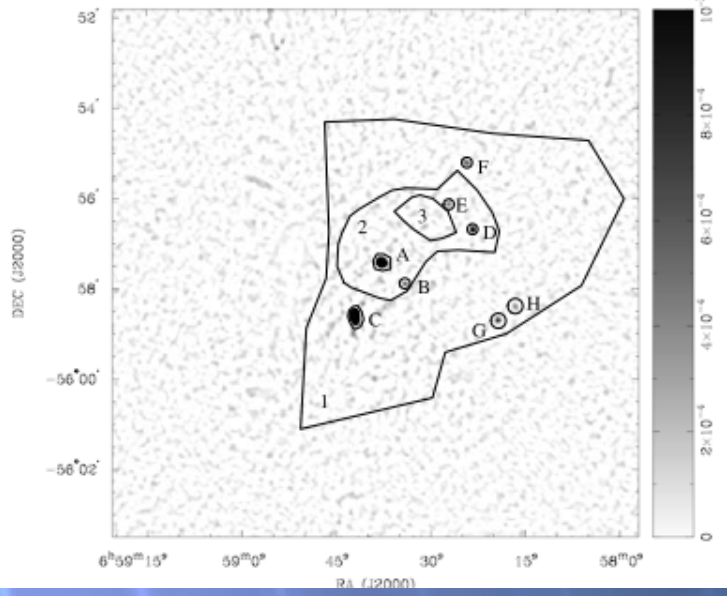

Atacama Pathfinder EXperiment APEX Telescope

Max-Planck-Institut für Radioastronomie

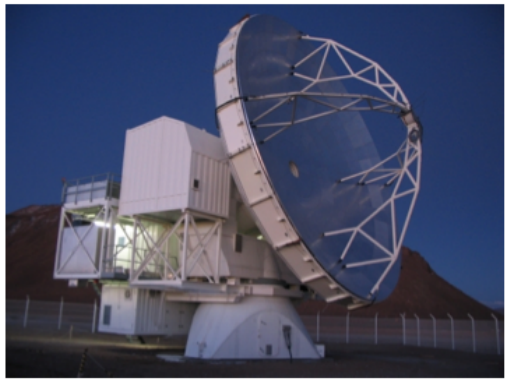

The APEX Telescope

Location	Llano de Chajnantor 50 Km east of San Pedro de Atacama, Northern Chile
Coordinates	Latitude : 23°00'20.8" South Longitude :67°45'33.0" West Altitude : 5105 m
Diameter	12 m
Mass	125000 kg
Main reflector	264 aluminium panels average panel surface r.m.s. 5 micron
Secondary reflector	Hyperboloidal Aluminium Diameter 0.75m
Mounting	Alt-Az
Surface	17 micron

Technical description of LABOCA

General

LABOCA is a multi-channel bolometer array for continuum observations. It operates in the 870 µm (345 GHz) atmospheric window. The array consists of 295 channels, which are arranged in 9 concentric hexagons around a central channel. The angular resolution is 18.6" (HPBW), and the total field of view is 11.4'. With a channel separation of about 36" (twice the beam size) the array is undersampled, thus special mapping techniques are used to obtain fully-sampled maps in a time-efficient manner.

The Bolometers

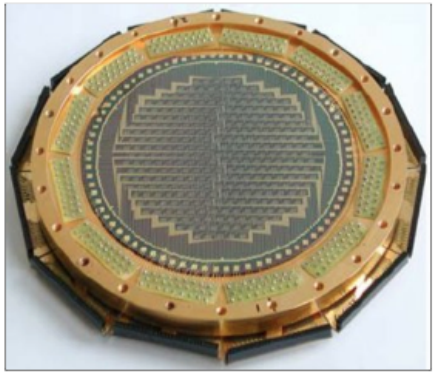

A bolometer is practically a thermometer. The radiation arriving at APEX from astronomical objects is absorbed by a thin metal film cooled to about 280 mK. This metal changes its temperature while absorbing the radiation, and this is measured by a heat-sensitive semiconductor. This results in a voltage change, which can be measured and amplified and is in principle proportional to the intensity of the incoming radiation.

For LABOCA, the thermal, electrical and mechanical structure of the bolometer array is based on a single silicon wafer. Free-

The 17 sources detected by APEX/LABOCA 850μm observations. The black contour shows the 2 mJy/beam level. The red inner dashed circle marks the 10 arcmin used for analysis (<z_{phot}> ~1.3, Rex et al. 2010). (185 scans/8 min int.)

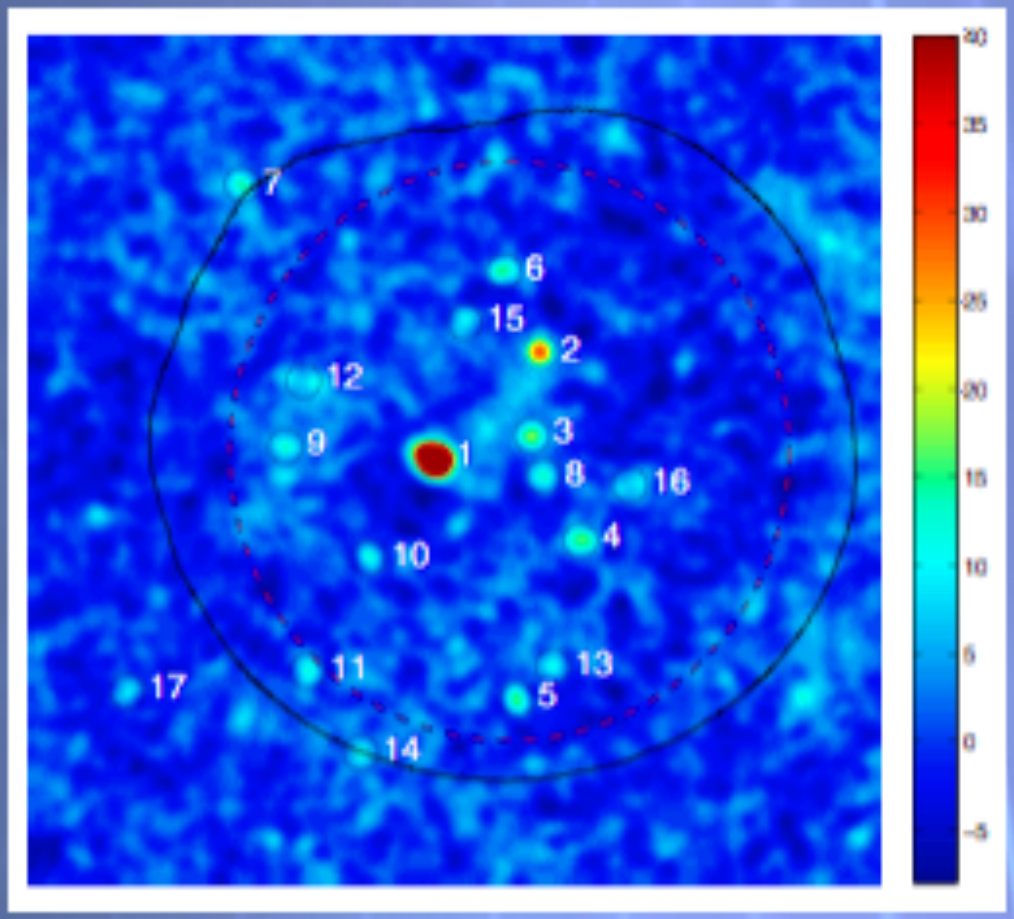

The GMF significance map, $F/\Delta F$, is computed as

$$\frac{F}{\Delta F} = \frac{(S \cdot W) \otimes P}{\sqrt{W \otimes P^2}} \quad (1)$$

where S is the signal map, W is the weight map (the reciprocal of the noise map, squared), and P is a Gaussian of the same size as the beam. The ⊗ sign denotes a convolution.

Johansson et al. 2010, A&A, 514, A77

Table 2. List of sources extracted from the LABOCA map.

Source	α(J2000) (h:m:s)	δ(J2000) (° ′ ″)	Flux density[a] (mJy)	Deboosted[b] flux density (mJy)	Demagnified[c] flux density (mJy)	$F/\Delta F$[d]
1	06:58:37.62	−55:57:04.8	48.6 ± 1.3[e]	48.0 ± 1.3	0.64	82.8
2	06:58:24.47	−55:55:12.5	15.1 ± 1.0	14.7 ± 1.0	8.8	29.9
3	06:58:25.45	−55:56:40.1	6.9 ± 0.9	6.4 ± 1.0	2.2	17.8
4	06:58:19.36	−55:58:30.3	8.2 ± 0.9	7.7 ± 0.9	4.7	16.2
5	06:58:27.27	−56:01:16.3	9.0 ± 1.3	8.0 ± 1.3	6.3	15.9
6	06:58:28.94	−55:53:48.4	9.3 ± 1.2	8.6 ± 1.2	6.3	15.4
7	06:59:01.39	−55:52:18.1	11.9 ± 2.1	9.7 ± 2.1	8.4	14.2
8	06:58:24.05	−55:57:23.0	5.3 ± 0.9	4.7 ± 1.0	1.8	13.1
9	06:58:55.98	−55:56:51.7	5.4 ± 1.2	4.4 ± 1.3	3.3	12.8
10	06:58:45.60	−55:58:48.0	6.2 ± 1.1	5.5 ± 1.1	3.6	12.0
11	06:58:53.22	−56:00:45.0	7.8 ± 1.5	6.4 ± 1.6	5.2	11.9
12	06:58:52.22	−55:55:45.7	5.5 ± 1.2	4.5 ± 1.2	3.4	11.2
13	06:58:22.88	−56:00:40.7	4.8 ± 1.2	3.8 ± 1.3	2.9	11.0
14	06:58:46.68	−56:02:11.8	7.2 ± 1.9	4.6 ± 2.5	3.8	10.8
15	06:58:33.69	−55:54:40.8	4.6 ± 1.1	3.6 ± 1.2	2.5	10.1
16	06:58:12.44	−55:57:29.7	4.9 ± 1.0	4.2 ± 1.0	1.9	9.2
17	06:59:15.72	−56:01:07.5	23.6 ± 5.9	[f]	–	9.0

Notes. Statistical uncertainties on the listed positions are 1–2″, which is smaller than the pointing uncertainty. [(a)] Flux density as extracted from the map. [(b)] Flux density corrected for boosting due to confusion noise. [(c)] Flux density corrected for lensing. [(d)] Significance of the detection in the Gaussian-matched-filtered map. [(e)] Source #1 is extended relative to the 22″ beam: it has an apparent size of 29.2″ × 23.3″. [(f)] Source #17 lies in the outer part of the map where the noise level is high and the method used to deboost the flux densities fails.

Johansson et al. 2010, A&A, 514, A77

APEX+LABOCA

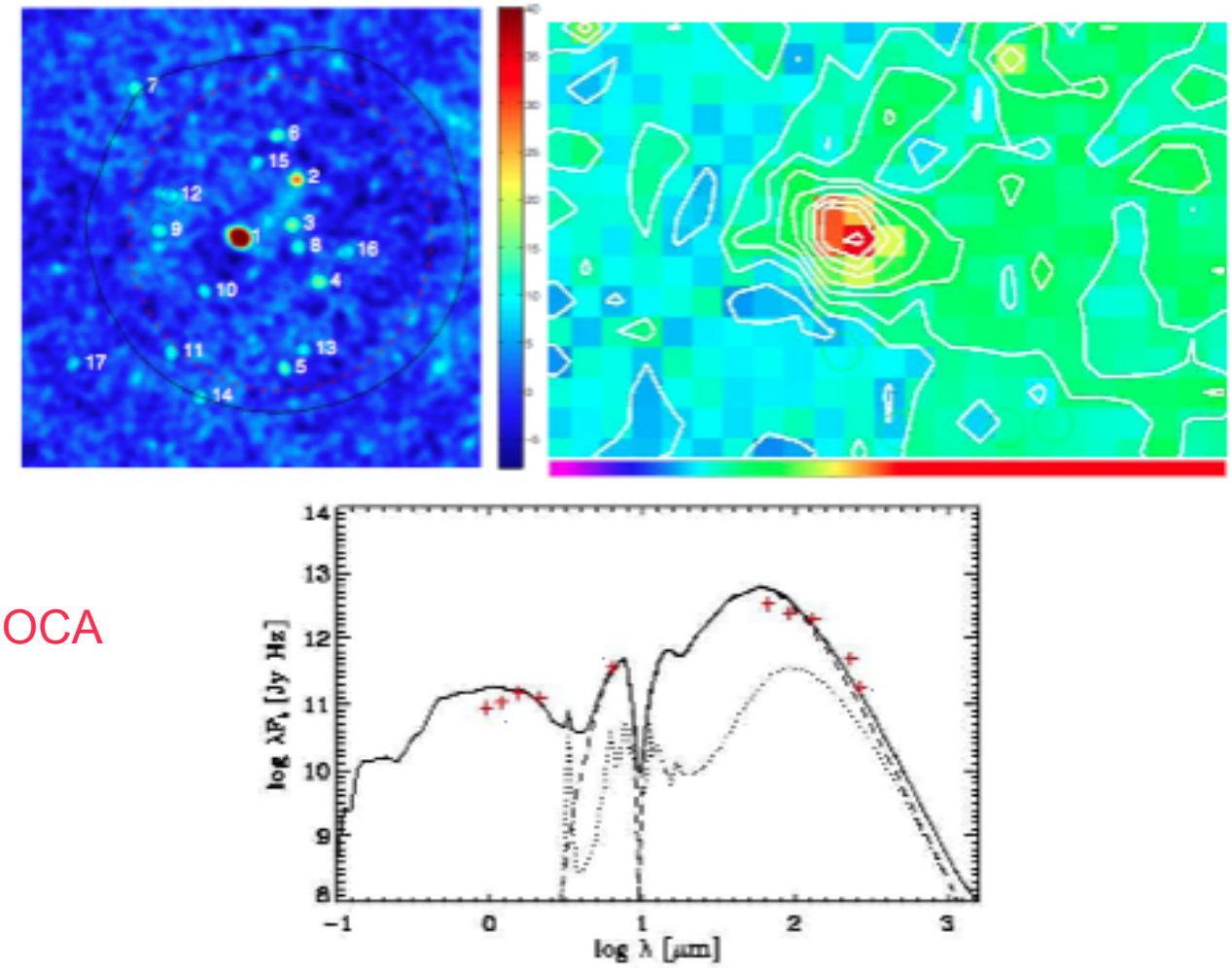

Figure 1: Figure 1a (upper left).- Gaussian filtered map generated from APEX+LABOCA observations at 870 μm. This map shows Source #1 with eleven further sources within the central 10-arcmin region of constant noise in the analysis of Johansson et al. (2010). Figure 1b (upper right).- Smaller region near Source #1, from an unsmoothed map generated from APEX+LABOCA observations at 870 μm, the faint extended Sunyaev-Zel'dovich effect signal is also visible (green). The resolution of 19.1 arcsec in this image is insufficient to resolve components A and B of Source #1. However the elongation of the contours is consistent with the positions of source A and B. Figure 1c (lower center).- Preliminary modeling of the rest-frame SED of Source #1 using GRASIL (Silva et al. 1998), with a renormalized flux density scale. Data-points are taken from Gonzalez et al. (2009), Rex et al. (2009), Johansson et al. (2010); and the revised measurement by Wilson et al (2009). The full data set cannot be modeled as a typical ULIRG.

The bullet has the most lensed galaxies

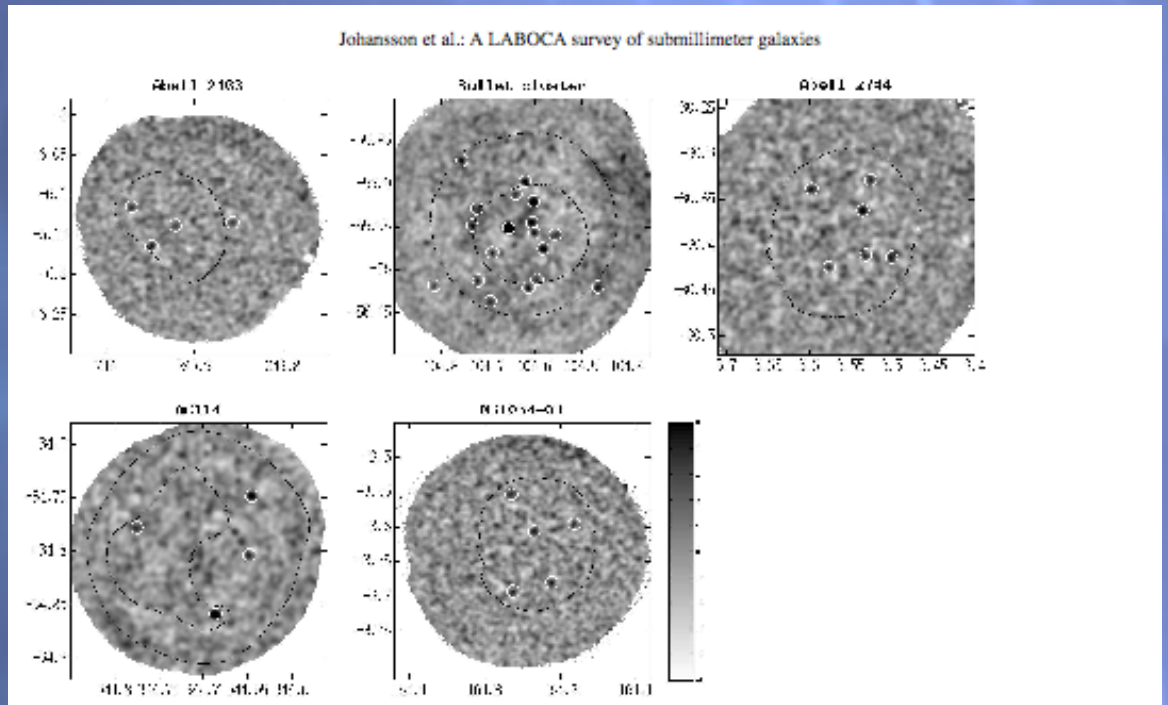

Fig. 1. Signal-to-noise maps of the five cluster fields. White circles represent the significant sources in the map and black contours show the noise maps of each cluster map at levels of 2, 4 and 8 mJy beam^{-1}. The signal-to-noise representation causes the appearance of the increasing noise towards the edge of each map to be suppressed.

Clusters observed with APEX/LABOCA by Johansson,Sigurdarson and Horellou (2011)

Target	α^a [J2000] [h m s]	δ^a [J2000] [° ′ ″]	z	rms^b [mJy beam^{-1}]	Ω^c [arcmin^2]
Abell 2163	16 15 45.1	−06 08 31	0.203	2.2	150
Bullet Cluster[1]	06 58 29.2	−55 56 45	0.296	1.2	220
Abell 2744[2]	00 14 15.0	−30 22 60	0.308	1.5	220
AC 114[3]	22 58 52.3	−34 46 55	0.312	1.2	130
MS 1054-03[4]	10 57 00.2	−03 37 27	0.823	1.6	200

Why the Bullet Cluster (1E0657-56)?

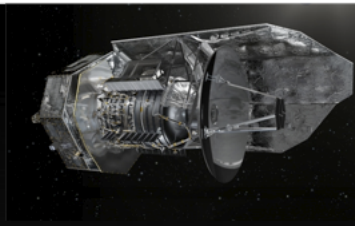

- Known bright, multiple-image, lensed submillimeter galaxy in the background (z=2.8; Bradac+06, Gonzalez+09, Rex+09)

- Recent collision of two clusters at z=0.3 (Markevitch+02,04)
  - Sub-cluster conveniently travelling perpendicular to our line of sight (<8° from sky plane)
  - Analysis of X-ray emission shows a supersonic bow shock proceeding the gas
  - Weak lensing maps indicate the X-ray gas lags behind the cluster galaxies due to ram pressure

- Abundant ancillary data:
  - multi-wavelength imaging
  - 930 spec-zs
    (mostly in cluster / foreground)
  - weak/strong lensing maps

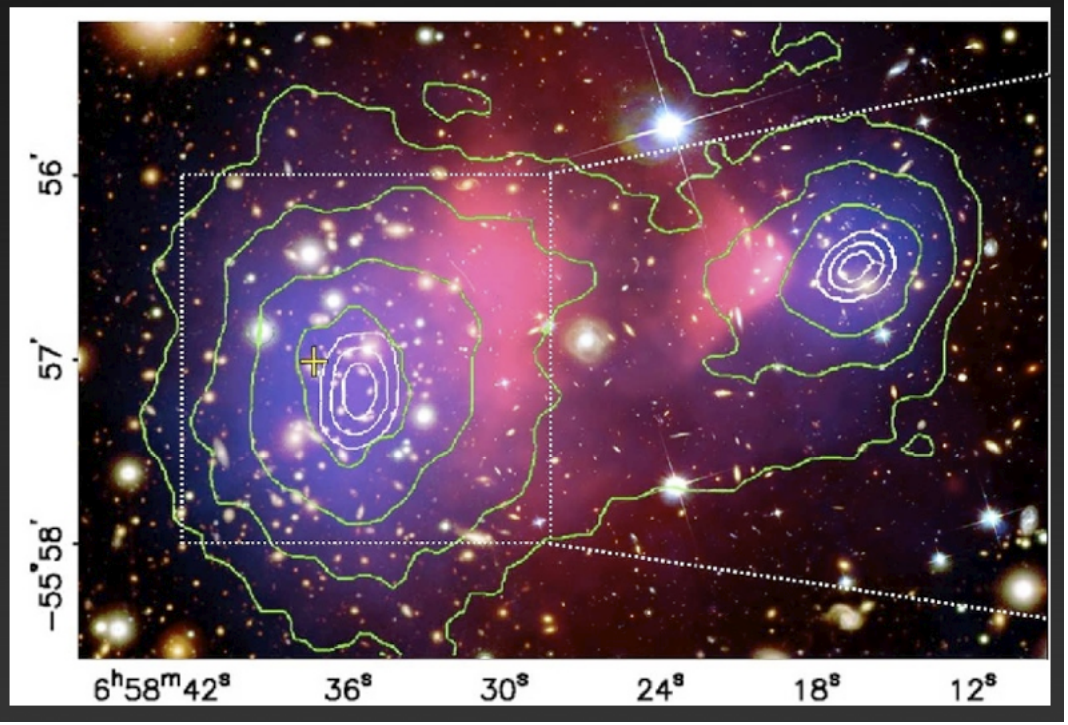

Clowe et al. (2004)
Rex et al. (2009)

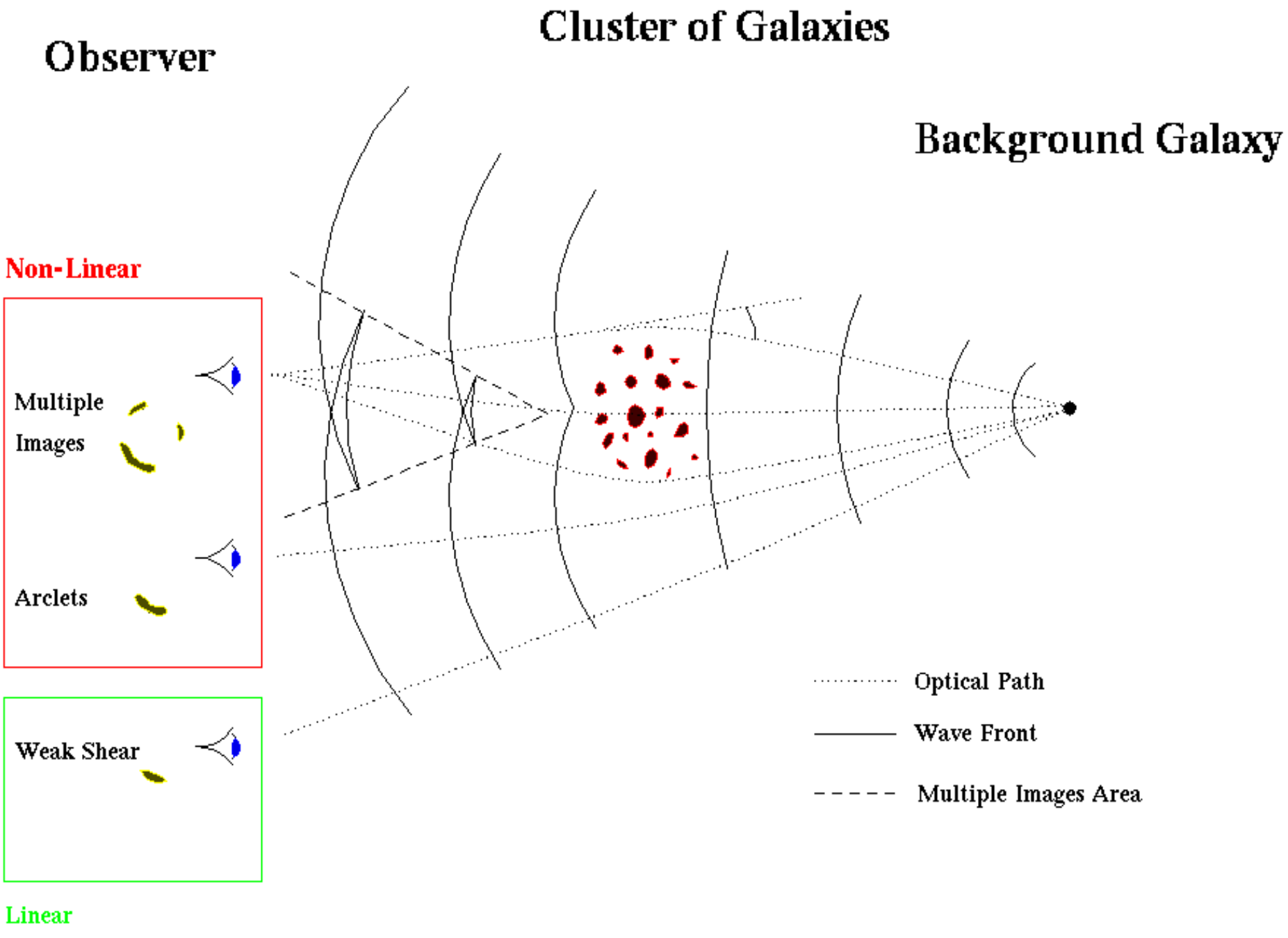
Observer
Cluster of Galaxies
Background Galaxy
Non-Linear
Multiple
Images
Arclets
Weak Shear
Linear
Optical Path
Wave Front
Multiple Images Area

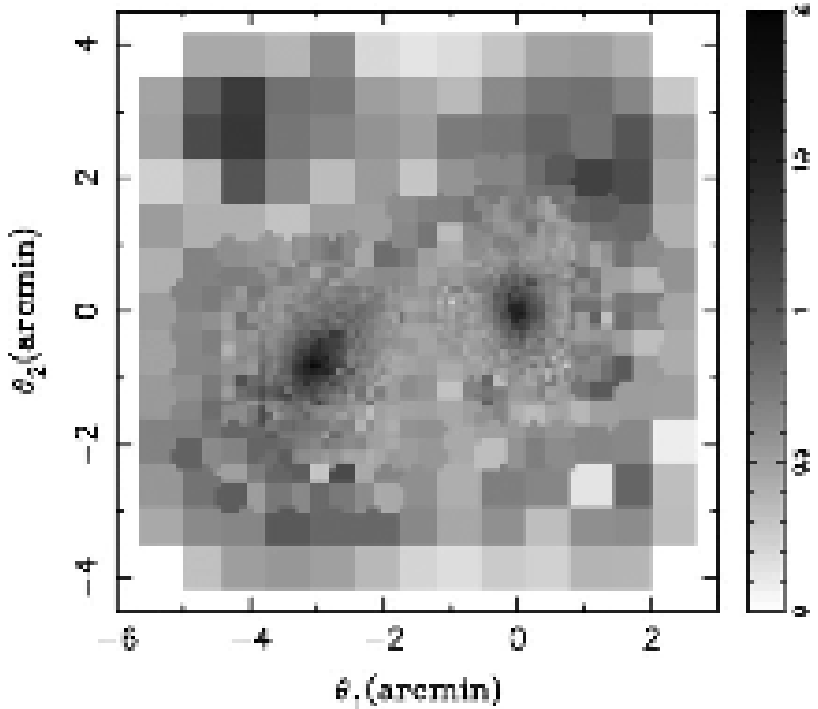

Figure 2. Reconstructed surface mass density κ of the cluster for a fiducial source at infinite redshift, $z_s \to \infty$.

Bradac et al., 2009

Gonzalez et al. 2009

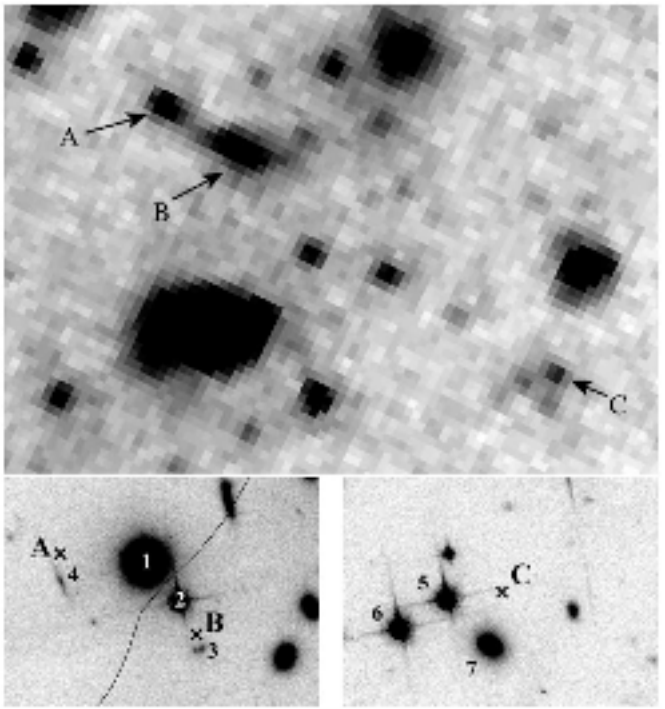

Figure 1. Top: 8 μm image showing the location of image C relative to images A and B. In this image the galaxy between images A and B has been subtracted for clarity. The field of view (FOV) is $65'' \times 50''$. Bottom: F850LP cutouts of the regions surrounding lensed images A and B (left) and image C (right). The crosses denote the locations of each image; the solid curve in the left panel is the critical curve from the $z = 2.7$ magnification map. The objects detected in the F850LP image that lie closest to the IRAC coordinates for images A and B are numbered 1–4. Object 1 is a cluster elliptical galaxy and object 2 is a star. The two fainter galaxies (3 and 4) are offset from the IRAC detections by $0''.8$ and $1''.5$, whereas the relative astrometry is good to $0''.25$, and can thus be excluded as optical counterparts to the lenses. The FOV is $17'' \times 12''$ in both panels. For all images north is up and east is to the left.

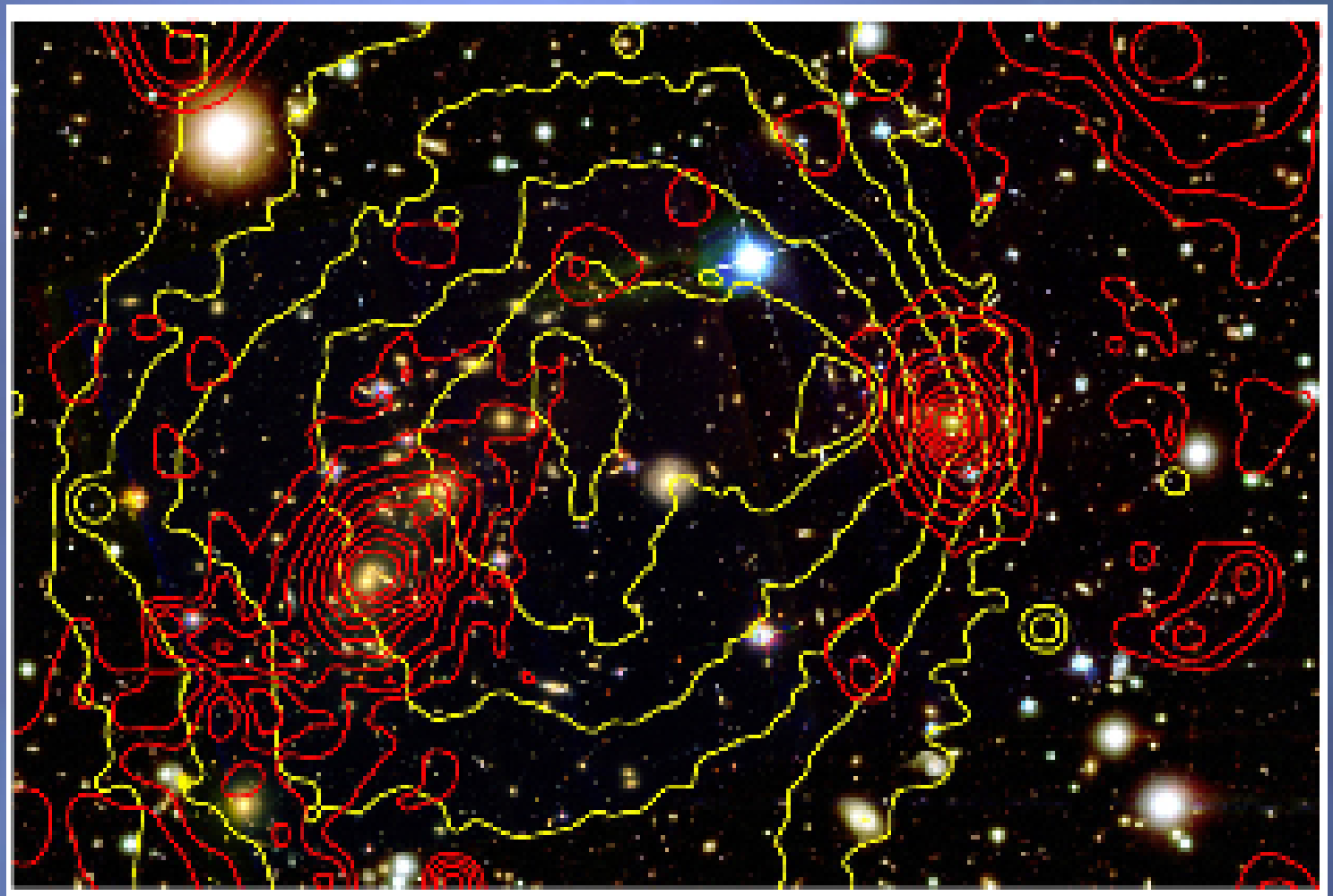

F435W−V−F814W (subcluster) color composite of the 1E0657 − 56. The ACS images are insr

Bullet Cluster

X-ray luminous cluster merger at $z = 0.3$

Special thanks...

Doug Clowe (Magellan/IMACS images)

Jean-Gabriel Cuby (VLT/HAWKI images)

Anthony Gonzalez, Sun Mi Chung (Magellan/IMACS redshifts)

Dario Fadda, Phil Appleton (CTIO Hydra redshifts)

Cathy Horellou, Daniel Johansson and LABOCA team

David Hughes, Itziar Aretxaga and AzTEC team

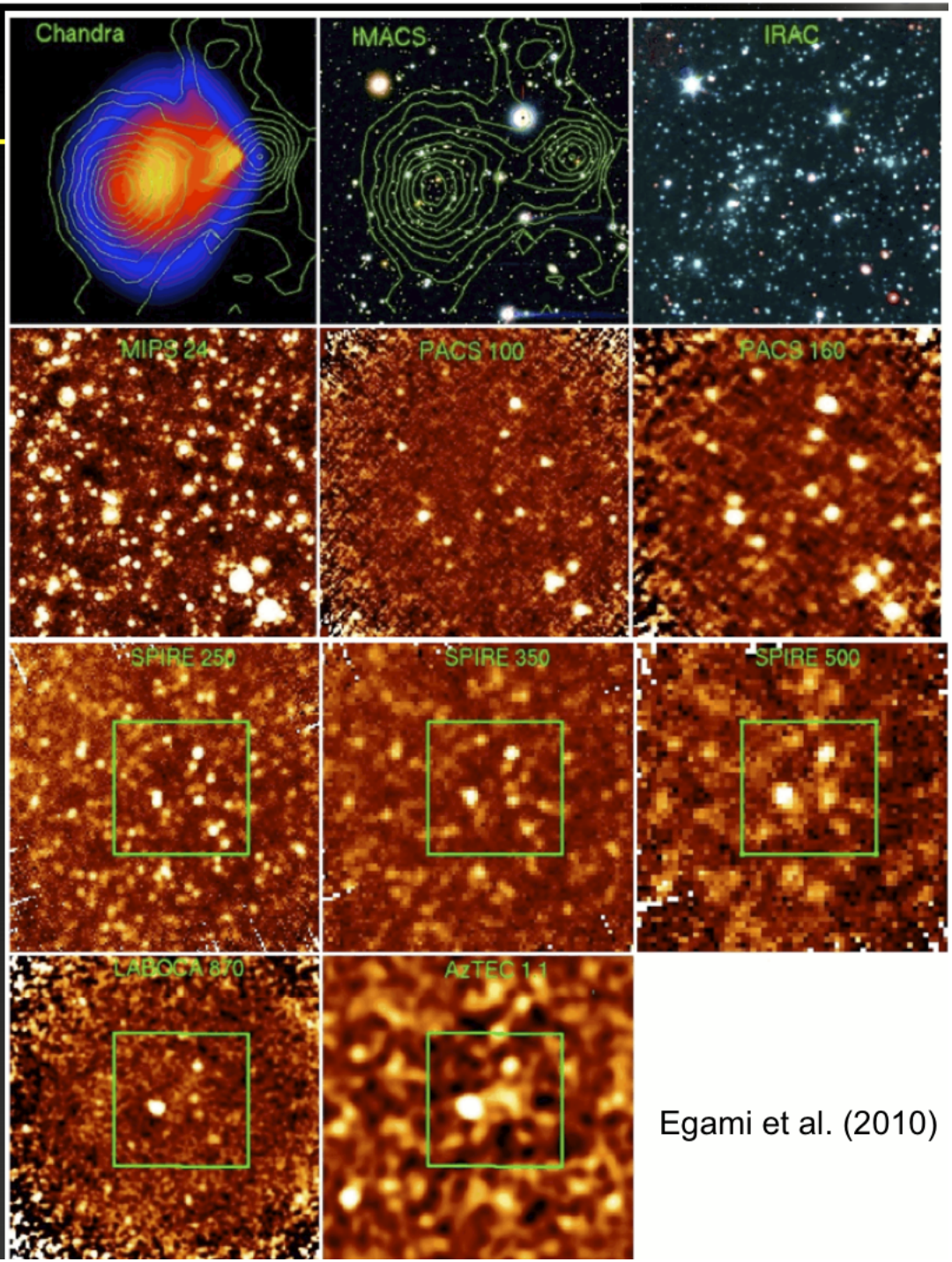

Egami et al. (2010)

BLAST vs SPIRE

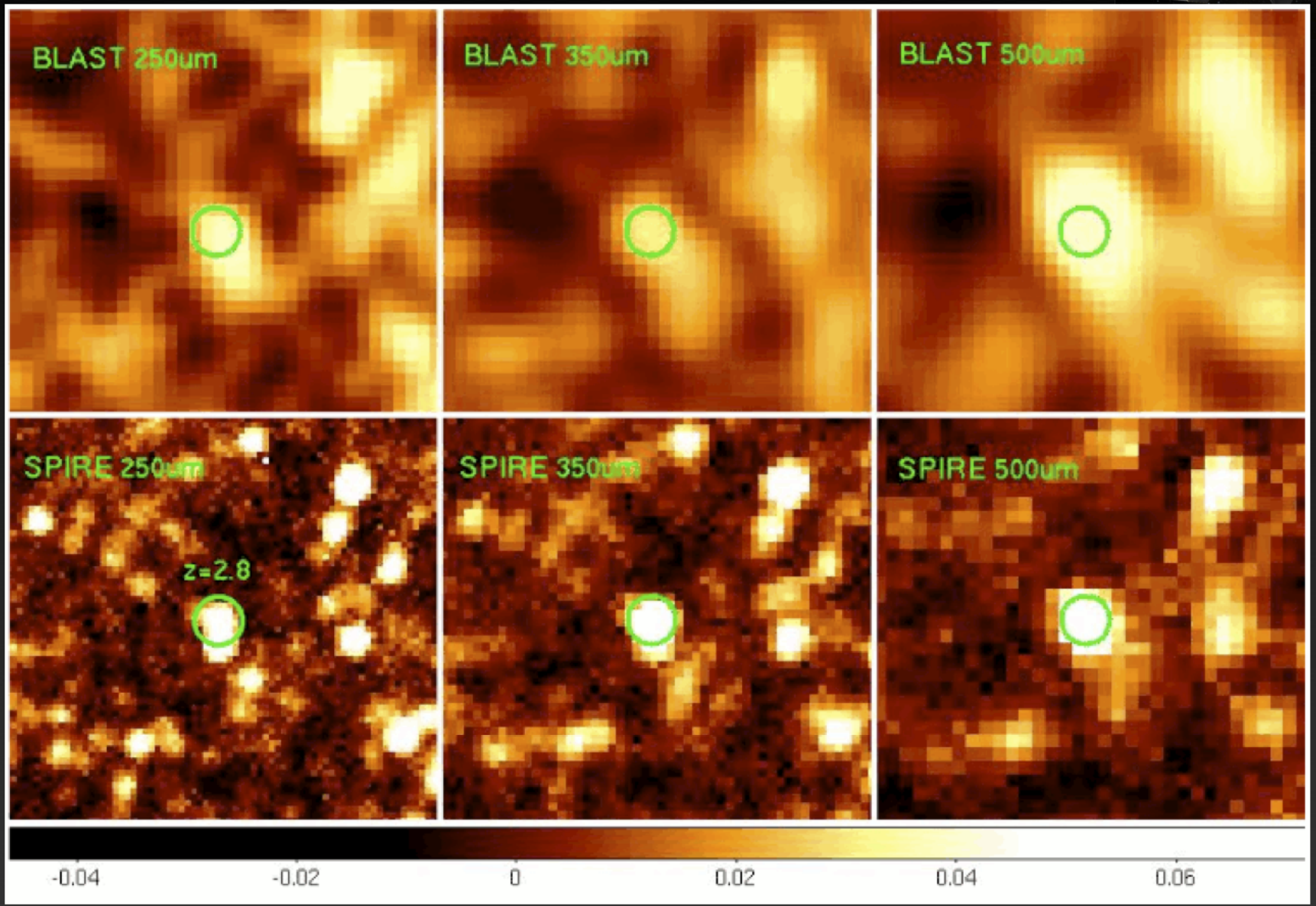

IR/submm SED of z=2.8 LIRG (5×10^{11} $L_\odot$)

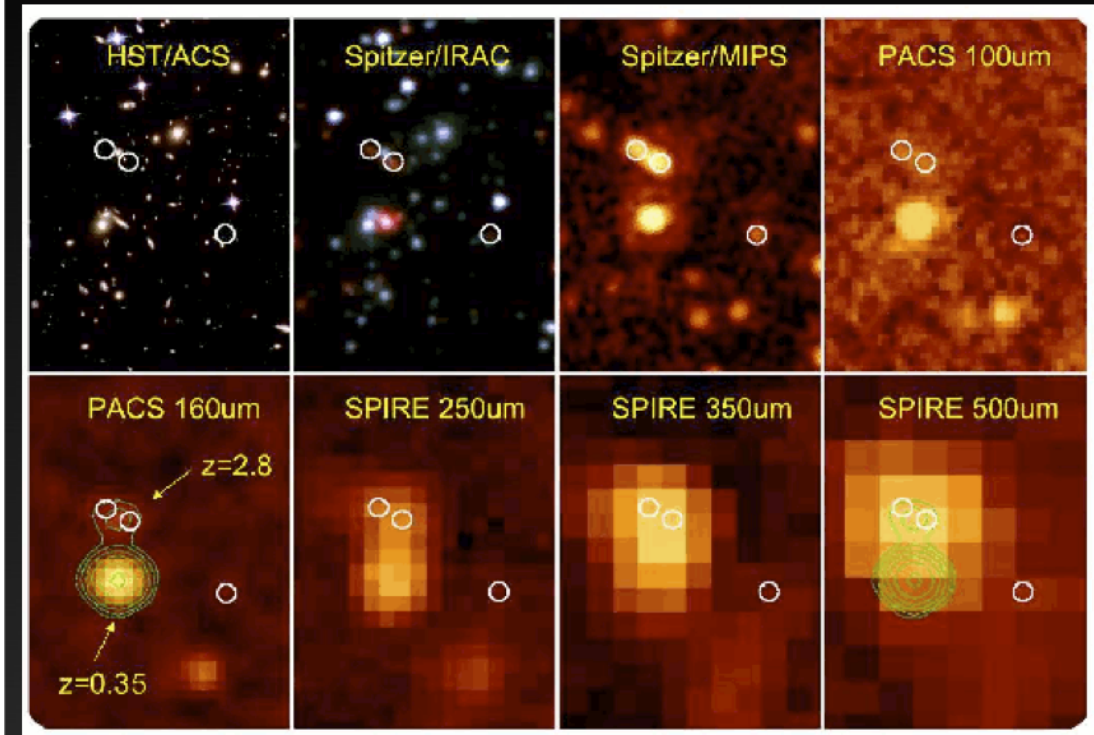

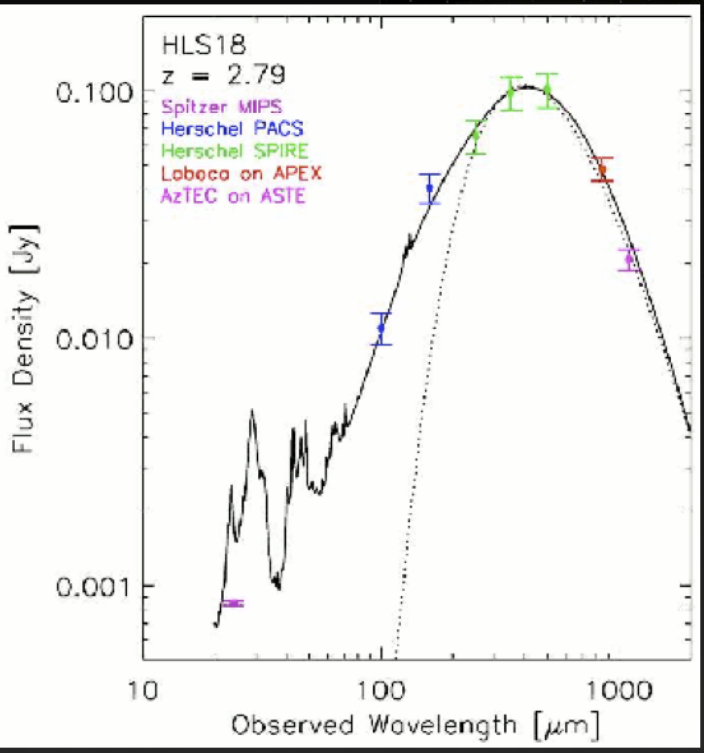

Rex et al. (2010)

Magnification factor 50x (→ 100x including unquantified local lensing)

- Observed flux densities: 7.0, 24.5, 65.3, 98.6, 101.4 mJy
- Corrected for lensing (x75): 0.09, 0.3, 0.9, 1.3, 1.4 mJy

Impossible to observe without lensing

CO redshifts for SMG

Schematic and now dated sub-mm spectrum of a molecular cloud showing fine structure & molecular emission lines (only the lowest rotational transition is shown).

Not all of the suggested species have been detected.

Phillips & Keene
Proc IEEE 80 1662 1992

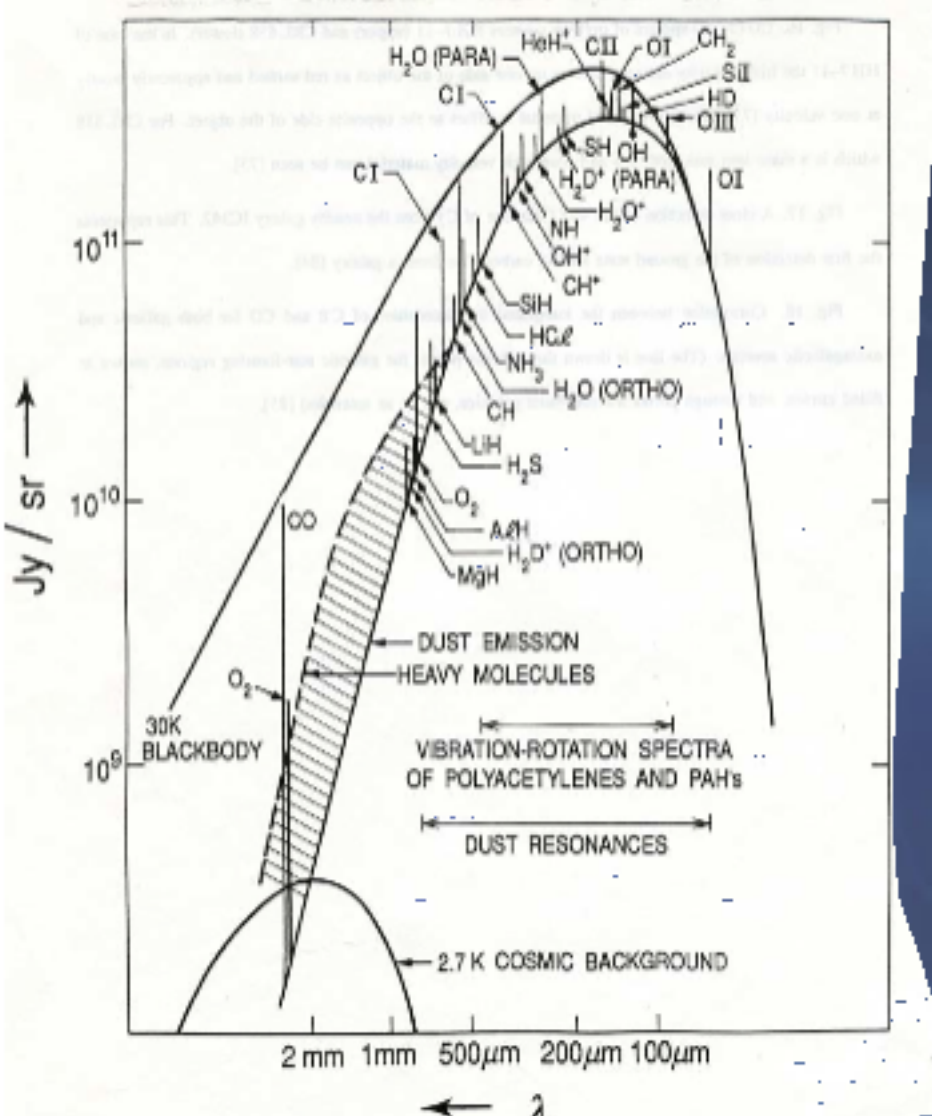

M82 reconstructed apodized spectrum

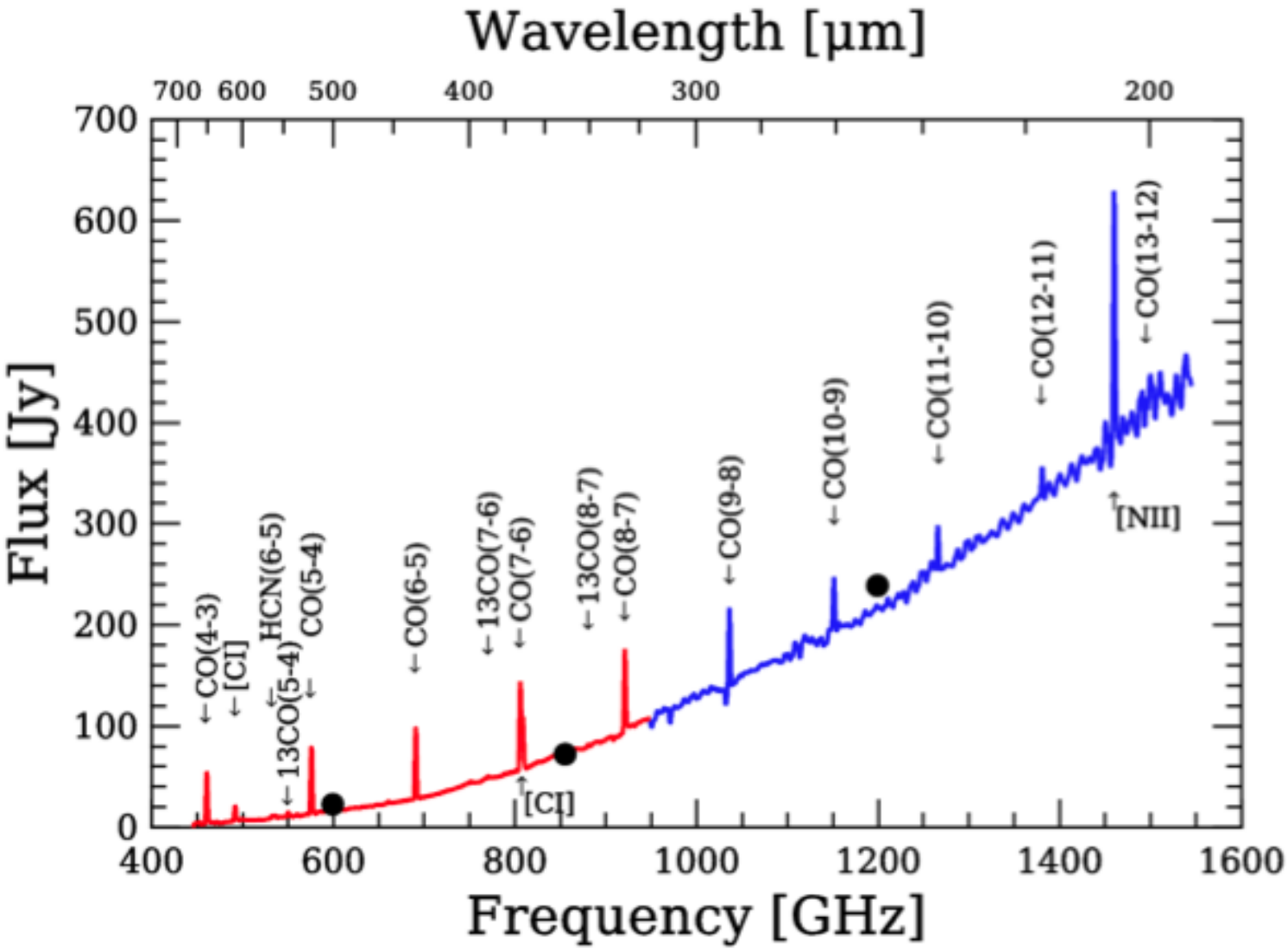

Gonzalez et al. 2010 PAH redshift, z=2.791 +/- 0.007

CO(3-2) ➔ 91.23 GHz; CO(1-0) ➔ 30.41 GHZ

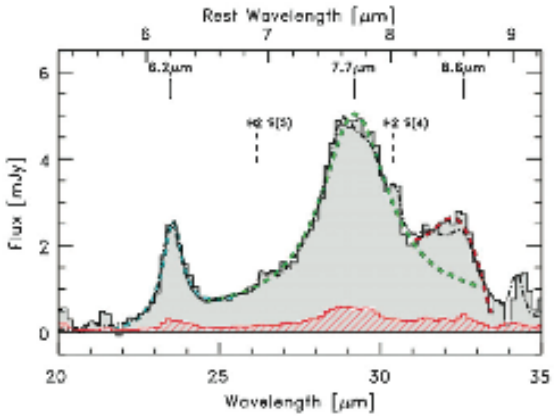

Figure 2. IRS spectrum of the galaxy, taken in the long-low mode. The data are presented as the shaded histogram, with the uncertainties shown by the hashed histogram. The dot-dashed line indicates the best fit from PAHFIT, while the dashed curves correspond to fits to the individual PAH lines using Drude profiles and the formulae from Smith et al. (2007). The vertical marks above the spectrum denote all spectral features robustly detected in our analysis.

(A color version of this figure is available in the online journal.)

Table 1
Observed Fluxes and Magnitudes[a]

Quantity	Value
$f(6.2\,\mu m)$	$1.4 \pm 0.2 \times 10^{-14}$ erg s^{-1} cm^{-2}
$f(7.7\,\mu m)$	$6.3 \pm 1.2 \times 10^{-14}$ erg s^{-1} cm^{-2}
$f(8.6\,\mu m)$	$5.2 \pm 3.3 \times 10^{-14}$ erg s^{-1} cm^{-2}
$f(H_2S(4))$	$5.8 \pm 1.9 \times 10^{-15}$ erg s^{-1} cm^{-2}
$f(H_2S(5))$	$2.5 \pm 1.2 \times 10^{-15}$ erg s^{-1} cm^{-2}
$f(7.7\,\mu m)/f(6.2\,\mu m)$	4.5 ± 1.1
m_{F160W}	23.80 ± 0.1 (AB)

Note. [a] All quoted values are for the combination of images A and B.

use a power law to fit the underlying continuum. We derive the redshift from the two strongest PAH features (6.2 μm and 7.7 μm), obtaining $z = 2.791 \pm 0.007$. This redshift confirms the photometric redshifts in the literature ($z \sim 2.7$–2.9; Wilson et al. 2008; Gonzalez et al. 2009; Rex et al. 2009).

The derived fluxes for the PAH features are listed in Table 1. The flux ratio for the two highest S/N lines, $f(7.7\,\mu m)/f(6.2\,\mu m) = 4.5 \pm 1.1$, can be compared with results from Pope et al. (2008) for SMGs. The star formation dominated SMGs in the Pope et al. sample ($z \sim 1$–2.5) have flux ratios in the range of 1.4–3.5 for these PAH lines, some

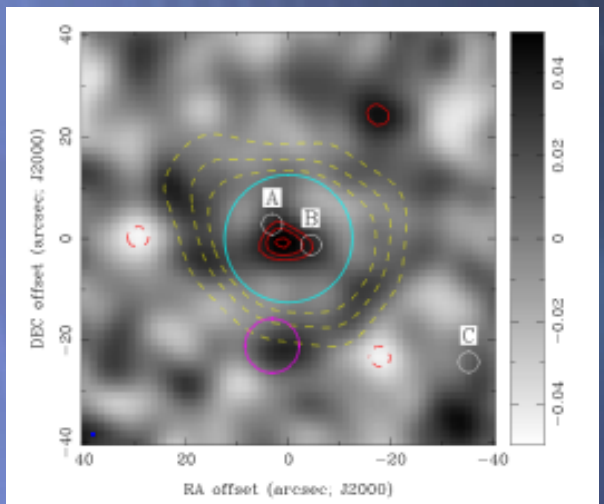

Fig. 2. Central region of the SABOCA 350 μm map. The grayscale is in Jy/beam. The red contours show significance levels of ±2.5, 3.0 and 3.5σ (positive values as solid lines and negative values as dashed lines). SMM J0658 is detected at the center of this image at 3.6σ significance. The white circles indicate the positions of the three Spitzer images A, B and C. The magenta circle has a diameter of 10.″6, the FWHM of the SABOCA image; it is located at the position of an infrared-bright elliptical galaxy at $z = 0.35$ (Rex et al. 2010) which is not detected by SABOCA, as expected. The yellow dashed lines correspond to the 3, 6 and 12σ levels of the LABOCA 870 μm detection. The source was detected by Herschel (Rex et al. 2010): the cyan circle shows the size of the Herschel beam at 350 μm (FWHM of 25″).

ATNF Facilities: ATCA 6 x 22m

CABB

Table 1. Some ATCA properties. — See the *ATCA Users Guide (Table 1.1)* for more details and up-to-date information.

ATCA observing bands	16-cm* (L/S)	6-cm (C)	3-cm (X)	15-mm (K)	7-mm (Q)	3-mm (W)
frequency range [GHz]	1.1 – 3.1	4.4 – 6.7	7.5 – 10.5	15 – 25	30 – 50	85 – 105
number of antennas	6	6	6	6	6	5
number of baselines	15	15	15	15	15	10
primary beam FWHM	44′ – 16′	10.′7 – 7.′4	6.′3 – 5.′1	∼2′	∼70″	∼30″

Notes: ATCA observing information can be found at *www.narrabri.atnf.csiro.au/observing*, including a link to the CABB Sensitivity Calculator which is highly recommended to obtain observing characteristics (e.g., $T_{\rm sys}$) at specific frequencies and correlator settings (see also Fig. 3). The ATCA primary beam size (in arcmin) can be approximated by $50/\nu$ where ν is the observing frequency in GHz; the MIRIAD task PBPLOT provides details of the primary beam model (see Fig. 4). * In 2010 the 1.5 GHz (20-cm) and 2.3 GHz (13-cm) bands were combined into one broad band covering the frequency range from 1.1 to 3.1 GHz (now referred to as the 16-cm band). Note that the 3- and 6-cm bands can be used simultaneously.

the ringing that was commonly seen with the original ATCA and other correlators while observing narrow spectral lines.

- Modes providing high velocity resolution (for spectral line studies), high time resolution (for the study of fast transients), or pulsar binning come as an addition to the basic wide-bandwidth modes.
- CABB also provides auto-correlation data.

These improvements have a major impact on the scientific ability of the ATCA (see examples in § 6), including the following:

- the much larger bandwidth reduces the time required to reach any particular continuum sensitivity, and the increased sampling depth allows for higher dynamic range and lower $T_{\rm sys}$;
- narrow, independent channels allow for precise excision of narrowband interference;

configuration	channel width	
	primary band	secondary band
CFB 1M–0.5k	1.0 MHz	0.488 kHz
CFB 4M–2k	4.0 MHz	1.953 kHz
CFB 16M–8k	16.0 MHz	7.812 kHz
CFB 64M–32k	64.0 MHz	31.250 kHz

Table 2. Basic CABB configurations.

Table 1. Parameters of the ATCA observations and data.

Phase center (J2000):	
Right ascension	$06^h58^m37\overset{s}{.}62$
Declination	$-55°57'04\overset{''}{.}8$
3 mm	
Configuration	214H
Bandpass calibrator	1921−293
Phase calibrator	0537−441
Primary flux calibrator	Uranus
Primary beam FWHM	$38''$
Synthesized beam[1]	$2\overset{''}{.}1 \times 1\overset{''}{.}7$; $82°$
Channel velocity width	3.3 km s^{-1}
Final velocity resolution	80 km s^{-1}
Noise level[2]	**1.6** mJy
7 mm	
Configuration	750A and 750D
Bandpass calibrator	0537−441
Phase calibrator	0724−47
Primary flux calibrator	Uranus
Primary beam FWHM	$110''$
Synthesized beam[1]	$5\overset{''}{.}5 \times 1\overset{''}{.}6$; $-8°$
Channel velocity width	9.8 km s^{-1}
Final velocity resolution	80 km s^{-1}
Noise level[2]	**0.85** mJy

The first 3mm CABB channel map. Observed on October 17-18, 2010 with ATCA

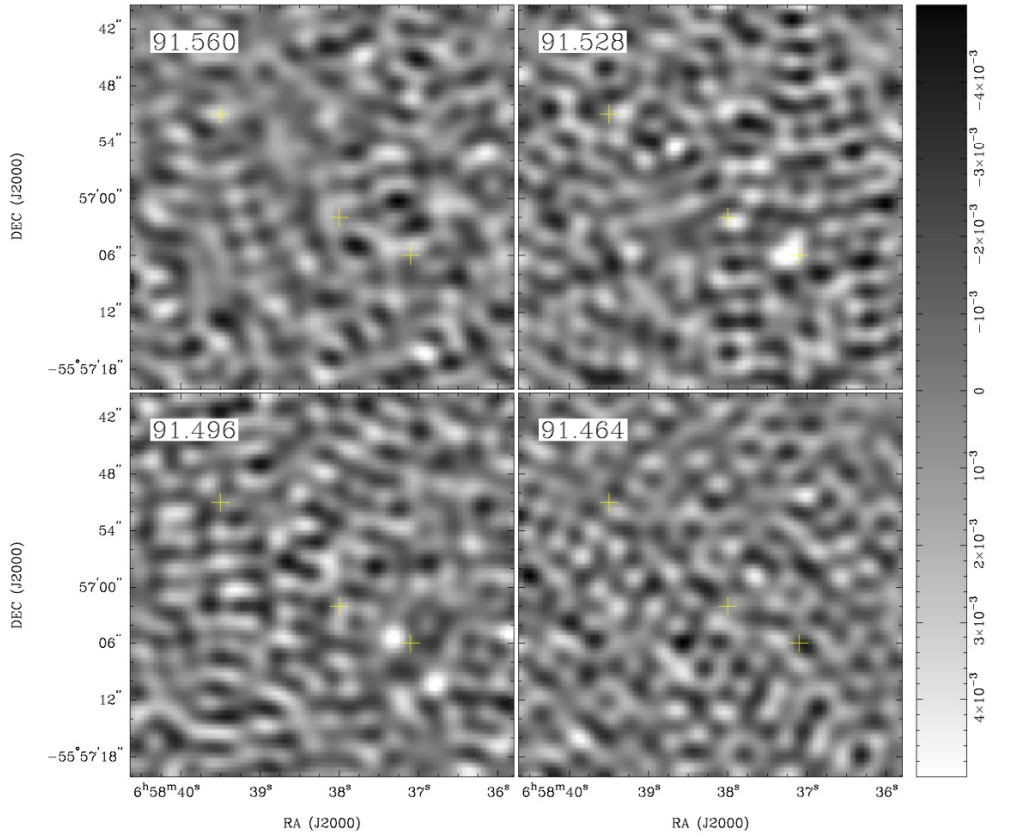

$$L_{\rm CO} = 3.25 \times 10^7 \, S_{\rm CO} \Delta v \, \nu_{obs}^{-2} \, D_L^2 (1+z)^{-3}$$

$$L_{\rm CO}\,[{\rm K\,km\,s^{-1}\,pc^2}]$$

(Solomon & Vanden Bout 2005)

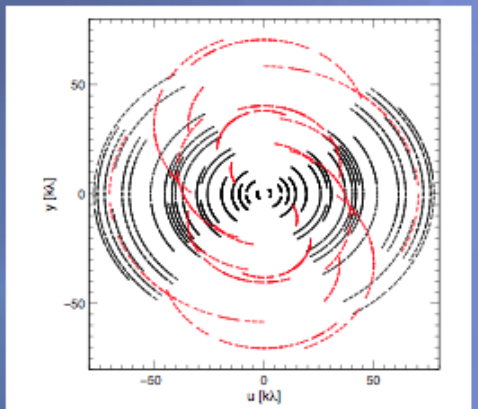

Fig. 3. *uv*-diagram showing the coverage of the 7 mm observations (black lines) and the 3 mm observations (red lines). The incomplete coverage in the 7 mm band (CO(1–0) observations) results in a more elongated beam.

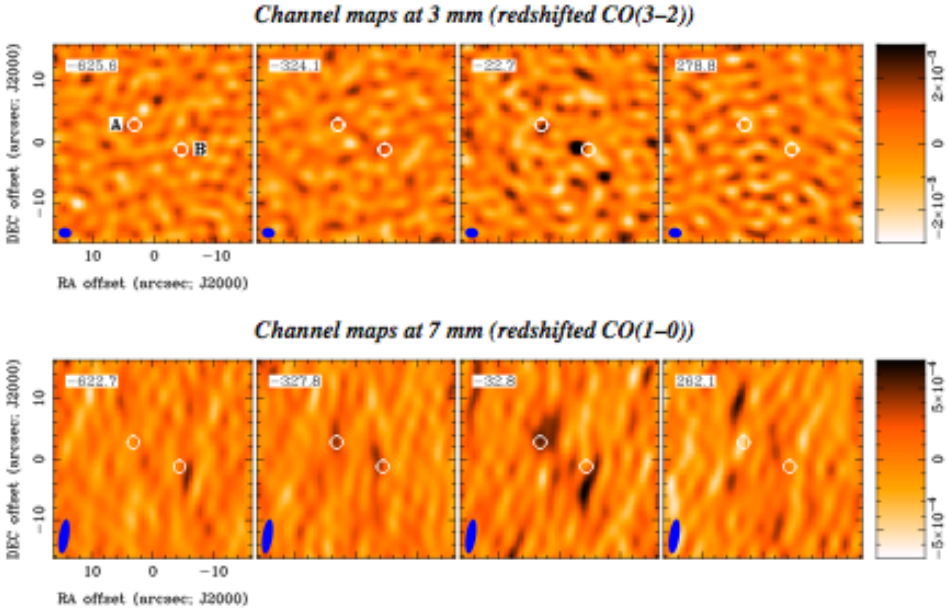

Fig. 4. Channel maps around the CO lines. The white circles indicate the positions of the Spitzer images A and B (G10). The central velocity of each channel is noted in the upper left corners. The channel width is ~ 300 km s^{-1}. The beam is shown in the bottom left corner and the color bars show the range of surface brightnesses, in Jy beam^{-1}. *Top row*: Channel maps at 3 mm, the band into which the CO(3–2) line is redshifted. Emission is clearly seen near image B (the western image) in the third panel. Faint emission near image A is seen in the third panel. *Bottom row*: Channel maps at 7 mm, the band into which the CO(1–0) line is redshifted. Emission is detected close to images A and B and is best seen in the third panel. The continuum source discussed in Sect. 3.2 lies outside the field displayed here.

Table 2. Integrated flux densities and upper limits on interesting molecular transitions in the ATCA bands.

		Image A	Image B	Image A+B	Image A+B	
Line	$\nu_{\rm rest}$	.....	Integrated flux	.....	$L_{\rm line}\,(\mu_{\rm AB}/100)^{-1}$	Flux B/A
	[GHz]		[Jy km s^{-1}]		[10^8 K km s^{-1} pc^2]	
^{12}CO(1–0)	115.271	0.34 ± 0.07	0.29 ± 0.07	0.63 ± 0.10	22.6 ± 3.6	$0.9^{+0.5}_{-0.3}$
^{12}CO(3–2)	345.796	0.94 ± 0.35	2.25 ± 0.35	3.18 ± 0.50	12.7 ± 2.0	$2.4^{+1.3}_{-0.7}$
HCN(4–3)	354.460	...	...	**< 0.7**	**< 2.7**	...
HCO$^+$(4–3)	356.734	...	...	**< 0.7**	**< 2.7**	...
CS(7–6)	342.883	...	...	**< 0.5**	**< 2.0**	...
		Brightness temperature ratios (r_{31})				
		$0.31^{+0.22}_{-0.14}$	$0.86^{+0.45}_{-0.28}$	$0.56^{+0.21}_{-0.15}$		

Notes. Uncertainties correspond to the 1σ level while upper limits are < 3σ. Integrated flux values are derived from fitting point sources at the positions of images A and B in the CO(1–0) and CO(3–2) maps collapsed for velocities between −350 and +170 km s^{-1}, as described in the text. This velocity range was determined from the spectral extent of the CO(3–2) spectrum.

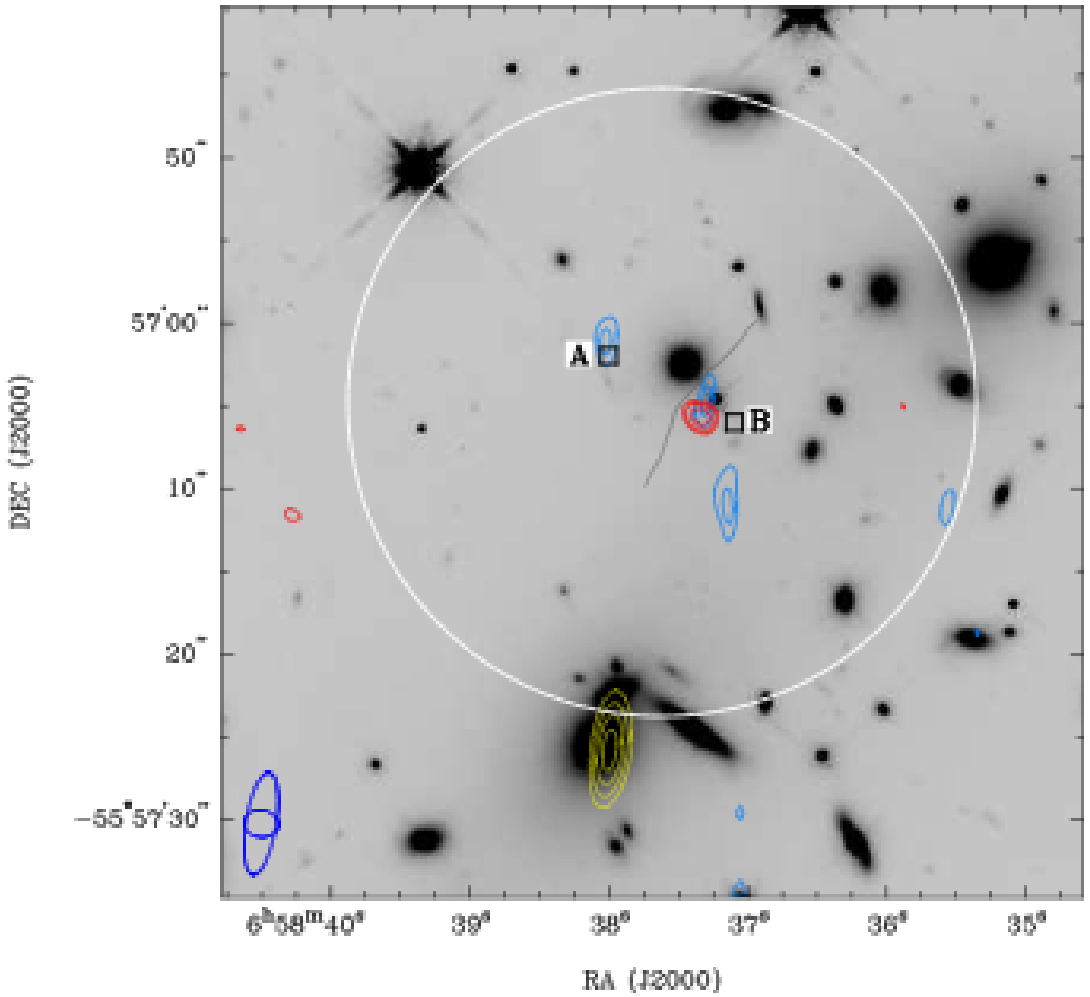

Fig. 5. Hubble Space Telescope WFC3 1.6 μm image of the region around SMM J0658. The blue contours show the CO(1–0) integrated intensity of both images of SMM J0658 and, red contours show the CO(3–2) integrated intensity. The 7 mm continuum emission from the $z = 0.35$ galaxy to the south is indicated by yellow contours. The two black squares indicate the locations of the two infrared Spitzer images, A to the east and B to the west (Gonzalez et al. 2009). **The gray line between images A and B is the critical line, derived from the lensing model for a source redshift of $z = 2.7$ (Gonzalez et al. 2009), very similar to the redshift derived from the CO observations.** The white circle shows the extent of the ATCA FWHM primary beam for the CO(3–2) observations; the primary beam at 7 mm is larger than the field displayed here. The offsets seen between the various components are discussed in Sect. 5.1.

fold arc

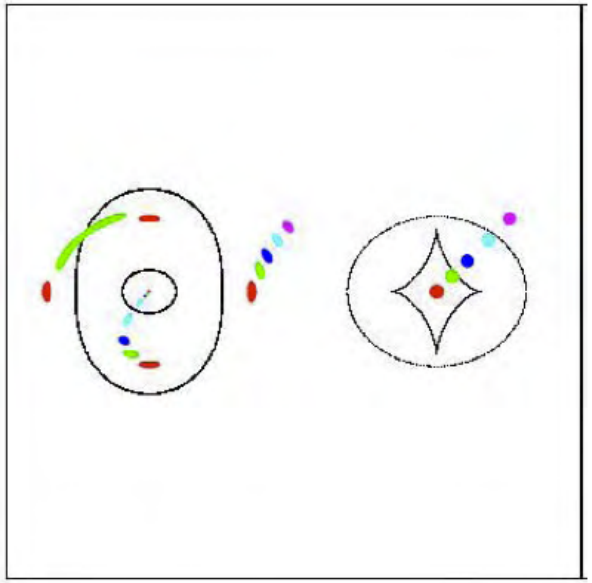

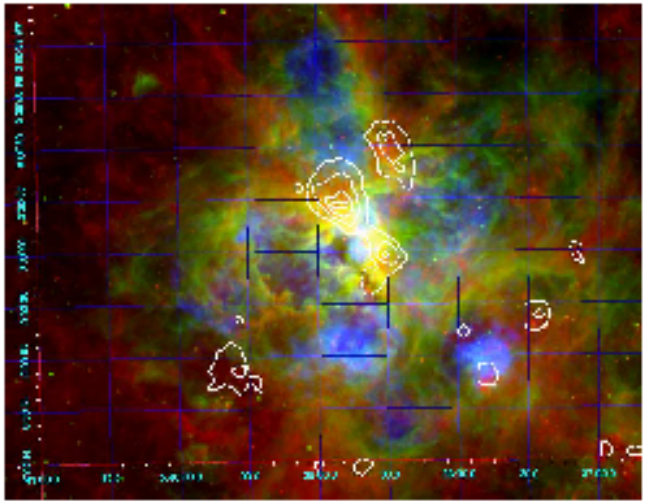

FIG. 2.— Three-color image of 30 Dor: MIPS 8μm (red), Hα (green), and 0.5-8 keV X-rays (blue). White contours show the ^{12}CO(1-0) emission (Johansson et al. 1998) in the region. Both large- and small-scale structures are evident. North is up, East is left.

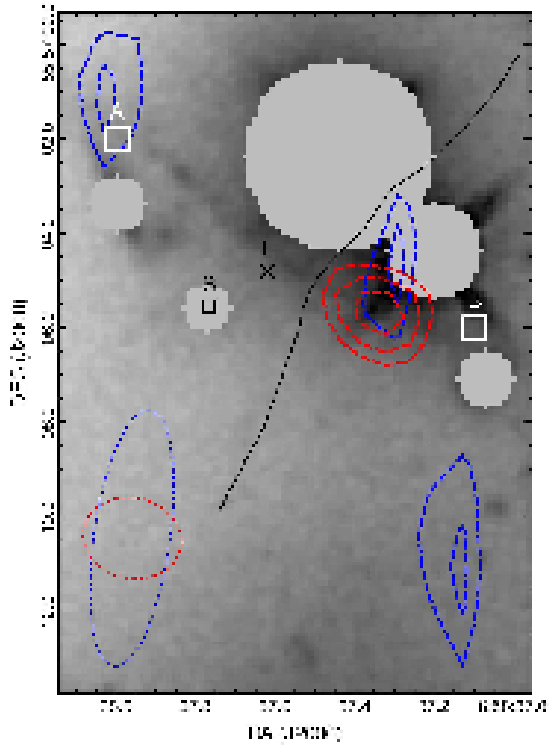

Fig. 8. HST image (G10) of SMM J0658 overlaid with the two Spitzer image positions A and B (**white squares**). **The red and blue contours are the same as in Fig. 5, and show the CO(3–2) and CO(1–0) emission.** We used GALFIT to subtract a model of the elliptical galaxy at (α_{2000}, δ_{2000})=**(06:58:37.44, −55:57:2.4)** and masked the region of that galaxy, **a nearby star and four other objects (gray disks)**. The faint arc between images A and B is visible, **roughly orthogonal to the critical line shown in black** (see Fig. 3 in G10 for a color image). The cross and box markers show the centroid of the LABOCA and SABOCA detections. **The synthesized beams at 3 mm and 7 mm are shown in the lower left corner as red and blue ellipses.**

z_{CO}=2.7795 +/- 0.0010 CO(3-2)/CO(1-0)=0.56

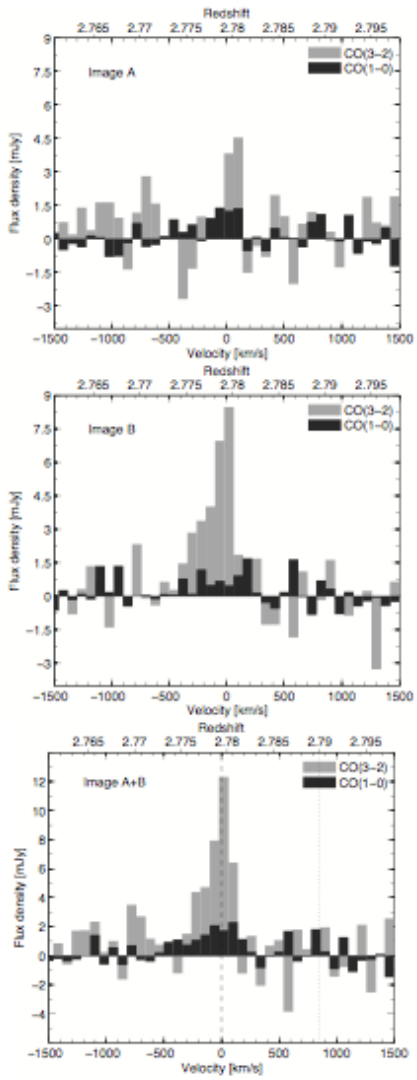

Fig. 6. CO(1–0) and CO(3–2) spectra as function of velocity and redshift, showing that both emission lines originate from gas at the same systemic velocity. The **upper and middle panels** show individual spectra toward the positions of image A and B. The lower panel shows the combined spectrum, in which we also indicat the derived redshift $z = 2.7795$ (dashed line) which is different from the redshift derived by G10 ($z \sim 2.79$, dotted line). The velocity resolution of both the CO(1–0) and CO(3–2) spectrum is 80 km s^{-1}. **Note that the *y*-axis scaling is different in the lower panel.**

Components at the same z; hence, we are dealing with a single galaxy.

Gas Mass and Dynamical Mass

CO-H_2 conversion.

Taking $M(\mathrm{H_2}) = \alpha L_{\mathrm{CO}}$

$$\alpha = 0.8 M_\odot (\mathrm{K\,km\,s^{-1}\,pc^2})^{-1}$$

$$M_{gas} = (1.8 \pm 0.3) \times 10^9 M_\odot$$

$$M_{dyn} = 1.16 \times 10^9 \left(\frac{\Delta V_{\mathrm{FWHM}}}{100\,\mathrm{km\,s^{-1}}} \right)^2 \left(\frac{\phi}{\mathrm{kpc}} \right) (sin\, i)^{-2}$$

Formula by Papadopoulos et al. 2000; taking <sin *i*> = 0.5; L = 2 kpc

$$M_{dyn} = (1.3 \pm 0.4) \times 10^{10} \left(\frac{L}{1\ \mathrm{Kpc}} \right) M_\odot$$

Dust Temperature

$$S_\nu = A\left(\frac{\nu}{\nu_o}\right)^{\beta} B_\nu(T_{\rm dust})$$

$$M_{\rm dust} = \frac{D_L^2 S_{\nu_{\rm obs}}}{(1-z)k_d(\nu_{\rm em})}\left[B(\nu_{\rm em}, T_d) - B(\nu_{\rm em}, T_{cmb}(z))\right]^{-1}$$

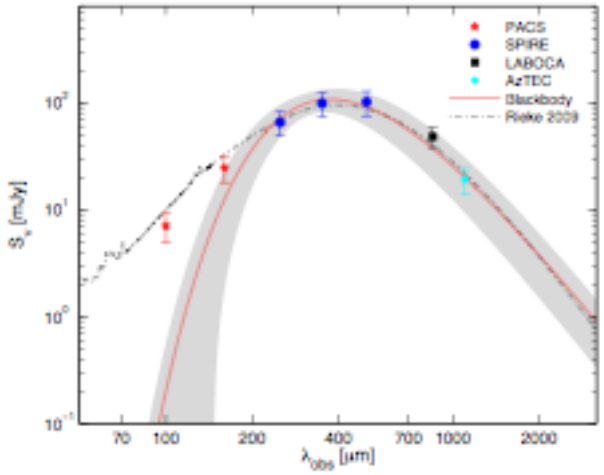

Fig. 7. Spectral energy distribution of SMM J0658. The solid line corresponds to the best-fit model of Eq. (3), with $\beta = 1.5$, and the shaded area is the 95% confidence intervals. The black curve is the LIRG template from Rieke et al. (2009).

T= 32.7 +\- 5.0 K

M_{dust}=1.7X10^7 $M_\odot$

Comparison with other highly magnify galaxies

Table 4. Summary and comparison of physical properties of SMM J0658 and other highly magnified SMGs.

Source	SMM J0658 (1)	SMM J16359+6612 (2)	SMM J2135−0102 (3)
Redshift	2.7795	2.5174	2.3259
Magnification	100	45	32.5 ± 4.5
Submm flux density (mJy)	~0.5	~0.8[a]	~ 3
$L_{CO(1-0)}$ (10^8 K km s^{-1} pc^2)	22.6 ± 3.6	–	173 ± 9
$L_{CO(3-2)}$ (10^8 K km s^{-1} pc^2)	12.7 ± 2.0	37 ± 2	117.6 ± 0.9
$M(H_2)$ (10^9 $M_\odot$)	2.3	4.5 ± 1.0	14 ± 1
M_{dyn} (10^9 $M_\odot$)	24	~ 30	~ 53
L_{FIR} ($10^{12}L_\odot$)	0.3	1.6 ± 0.4	2.3 ± 0.1
SFR ($M_\odot$ yr^{-1})	100 – 150	~ 500	400 ± 20
SFE ($L_\odot M_\odot^{-1}$)[b]	170	~ 320	165 ± 7
M_{dust} (10^7 $M_\odot$)	1.1	1.9 ± 0.3	~ 15
T_{dust} (K)	32.7 ± 5.0	51 ± 3	30; 57 ± 3

Notes. All values have been corrected for the individual gravitational magnification factors. [a] Flux density measured at 850 μm while the other two flux densities were measured at 870 μm. For a submm spectral index of ~ 3 the flux difference between the two wavelengths is less than 3%.
[b] Star formation efficiency, defined as $L_{FIR}/M(H_2)$
(1) This work.
(2) Kneib et al. (2004, 2005).
(3) Danielson et al. (2010).

D. Johansson et al.: Molecular gas and du

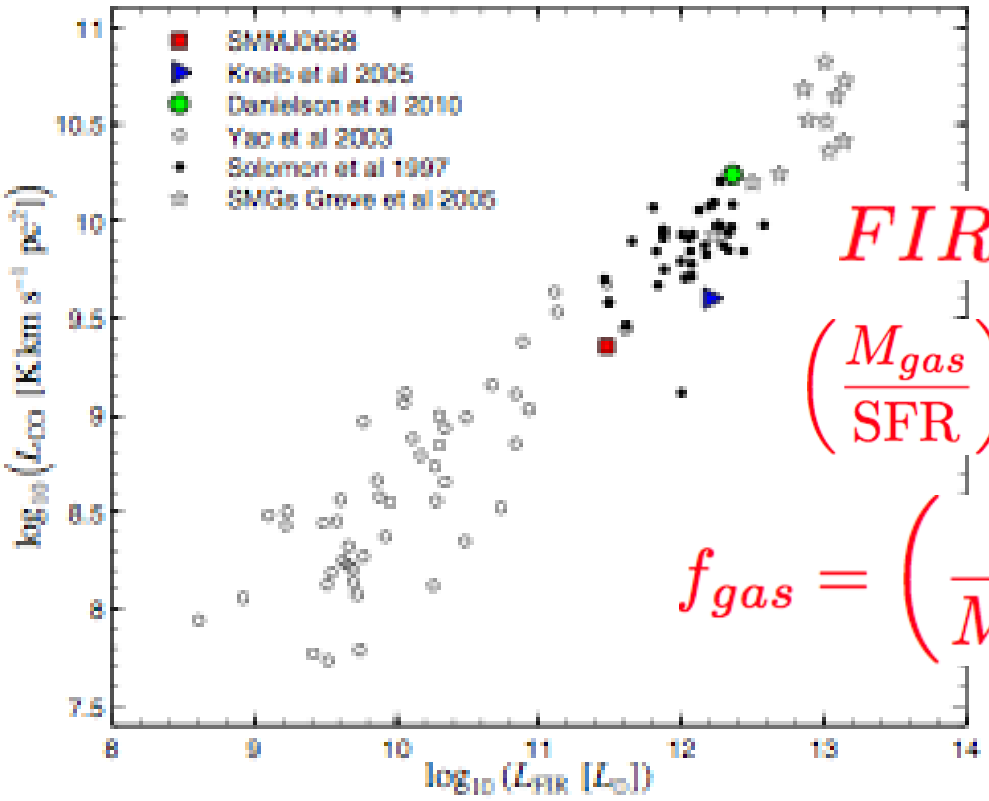

Fig. 9. Far-infrared luminosity versus CO(1–0) luminosity for SMM J0658, SMM J16359+6612 (Kneib et al. 2005) and SMM J2135–0102 (Danielson et al. 2010) (the three galaxies summarized in Table 4). Local luminous infrared galaxies (Yao et al. (2003),Solomon et al. (1997)) and high-redshift submm galaxies (Greve et al. 2005) are also shown. SMM J0658 is the least FIR-luminous high-redshift galaxy.

$$FIR \Rightarrow 100 - 150\ M_\odot yr^{-1}$$

$$\left(\frac{M_{gas}}{\mathrm{SFR}}\right) \Rightarrow Starbursting\ 15 - 20\,\mathrm{Myr}$$

$$f_{gas} = \left(\frac{M_{gas}}{M_{gas} + M_*}\right) = 31 \pm 12\%$$

$$f_{\mathrm{gas}}(\mathrm{local\ spirals}) \sim 7\%$$

SMG are usually ULIRGS

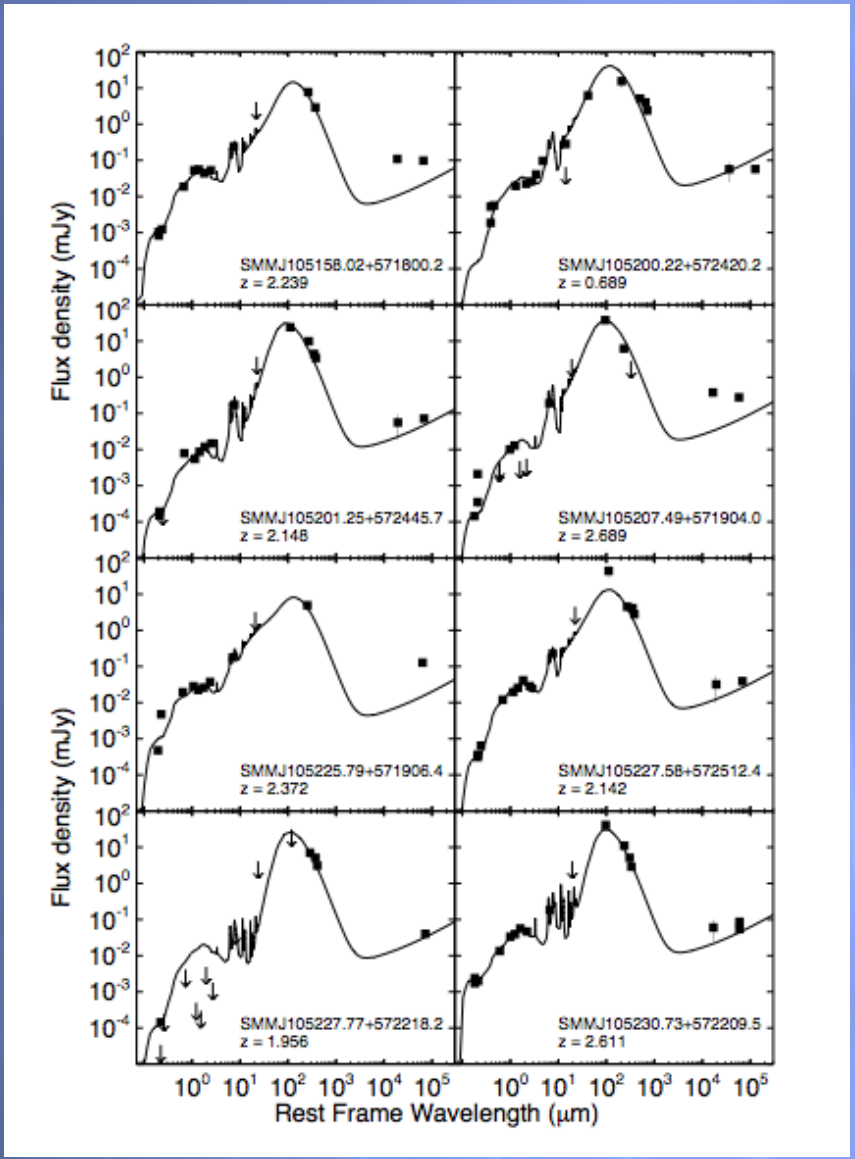

Michalowski et al. 2010

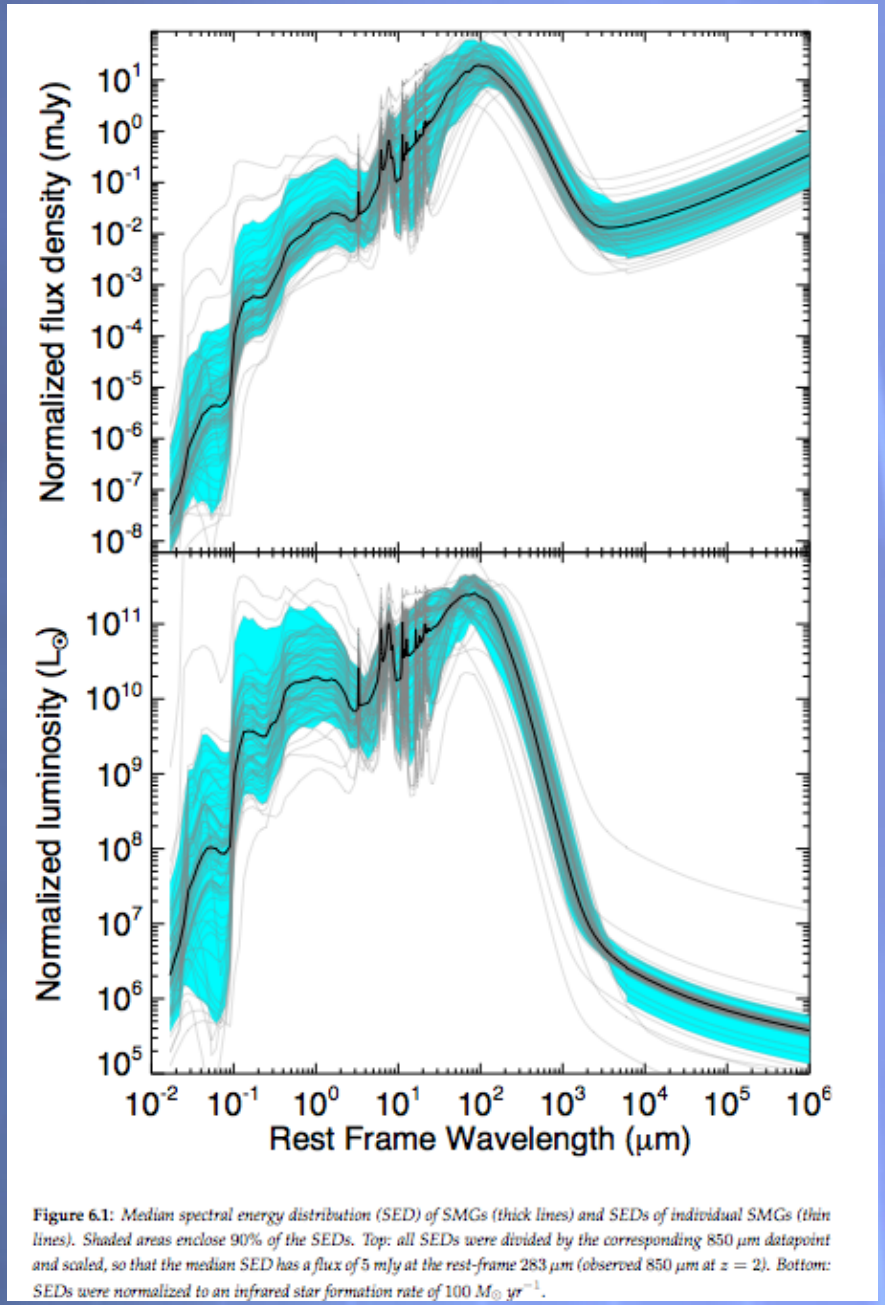

Figure 6.1: *Median spectral energy distribution (SED) of SMGs (thick lines) and SEDs of individual SMGs (thin lines). Shaded areas enclose 90% of the SEDs. Top: all SEDs were divided by the corresponding 850 μm datapoint and scaled, so that the median SED has a flux of 5 mJy at the rest-frame 283 μm (observed 850 μm at $z = 2$). Bottom: SEDs were normalized to an infrared star formation rate of 100 $M_\odot\ yr^{-1}$.*

Michalowski et al. 2010

Far-IR/submm template SEDs

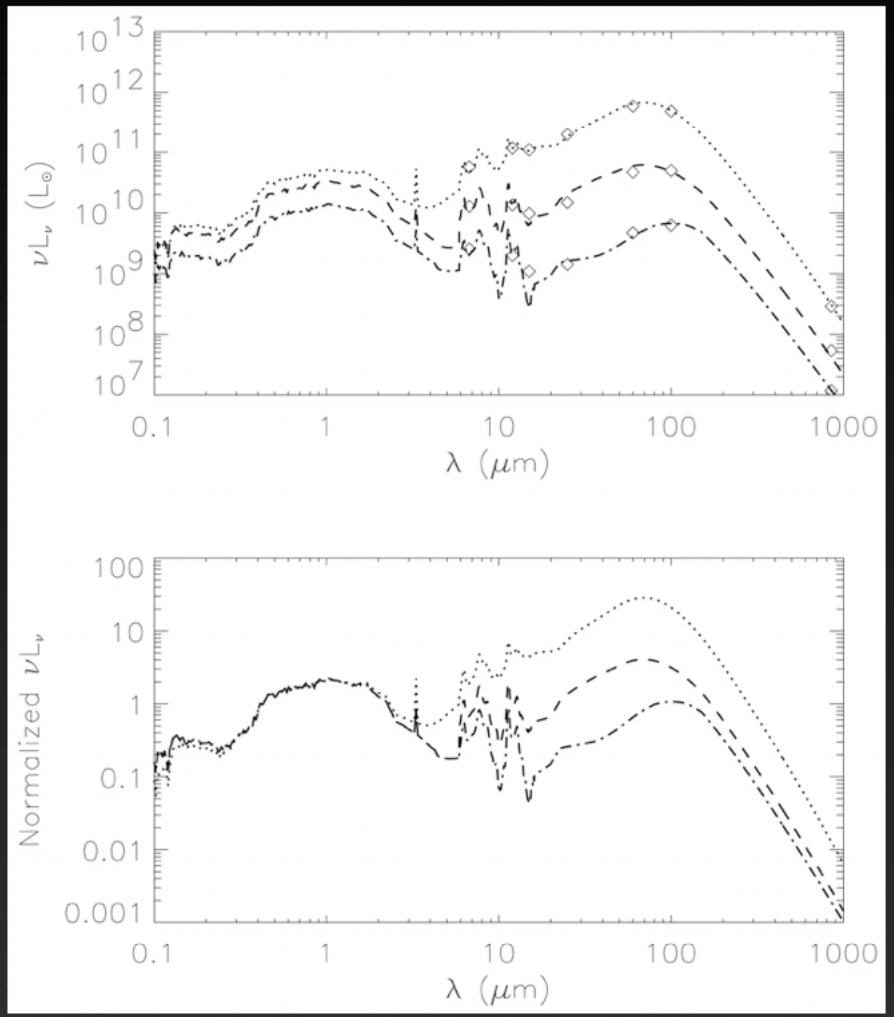

Chary & Elbaz (2001)

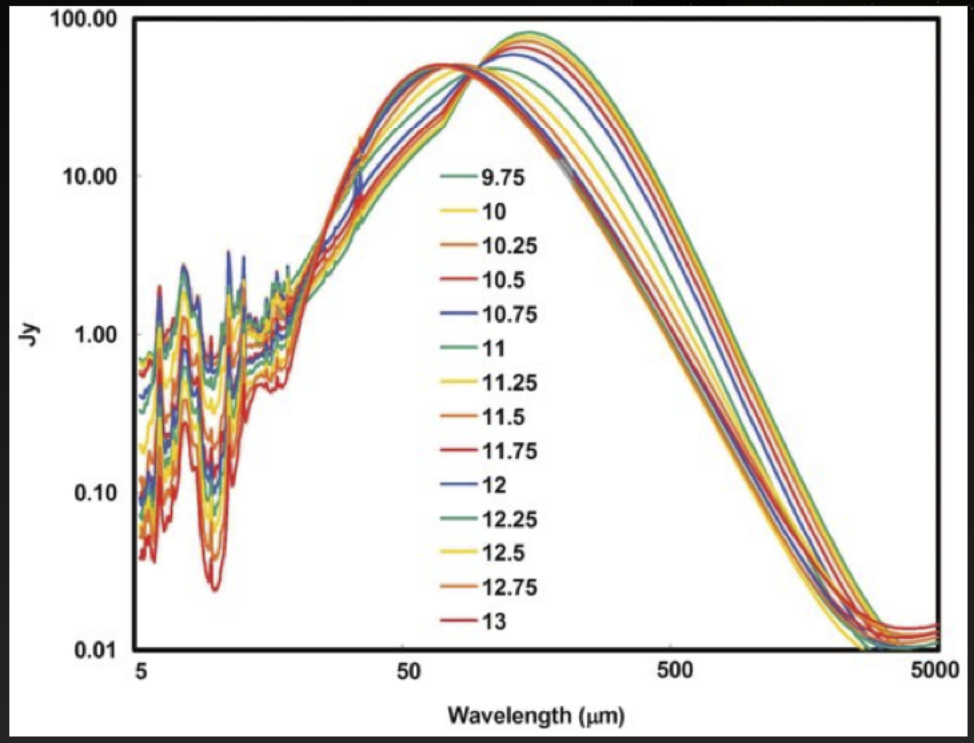

Rieke et al. (2009)

L_{TIR} ↑ ⇒ T_{dust} ↓ ⇒ L_{FIR}/L_{MIR} ↑

Do these local templates adequately describe high-z galaxies?

SMM J0658 SED

Published observation, modeled with GRASIL in progress

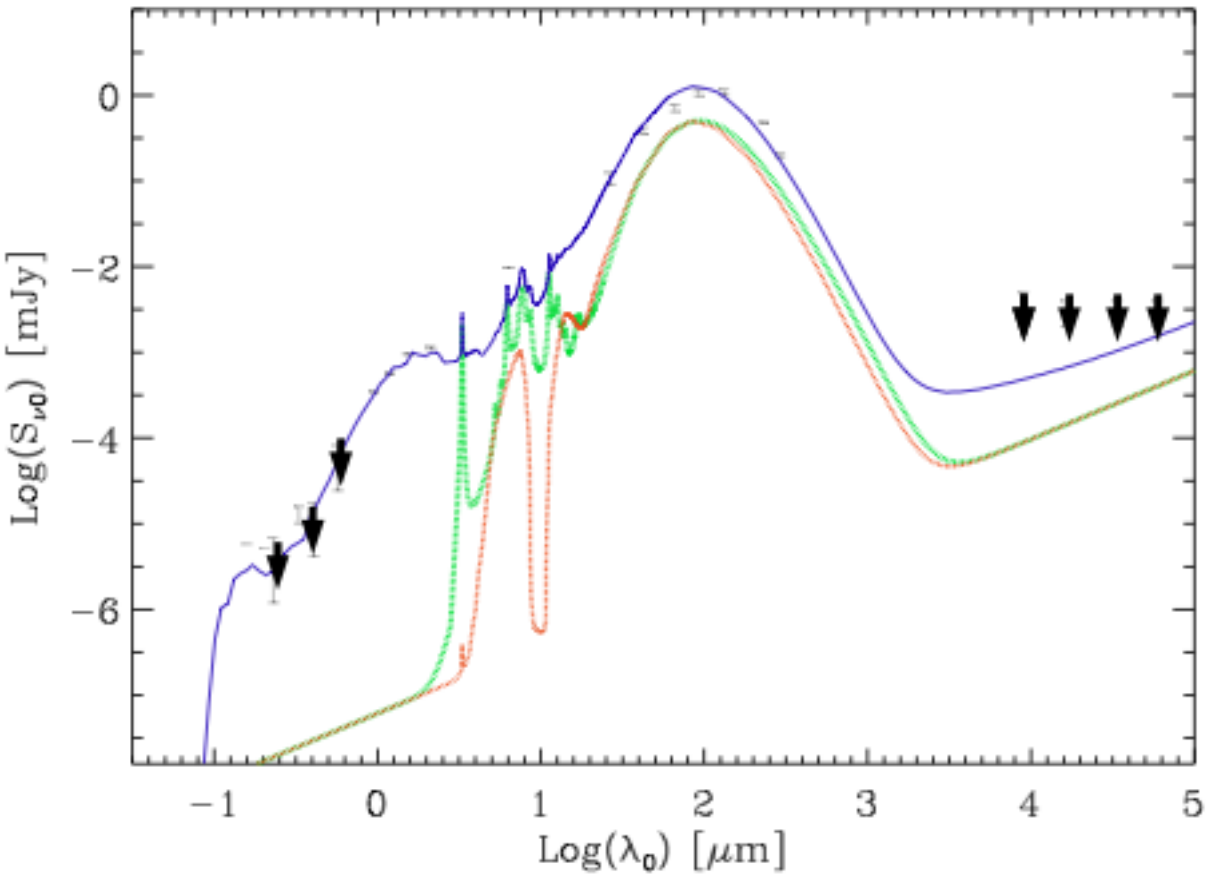

Conclusions

- Clusters of galaxies acting as natural telescopes allow us to study intrinsically faint SMG.
- We have detected CO for the first time using ATCA/CABB. We have refined on the redshift on the brightest SMG behind the bullet cluster.
- The derived masses are consistent with galaxies smaller than the Milky Way. SMM J0658 is an starbursting young galaxy. It may be more representative of the overall population of galaxies at z ~3.
- Observations with ALMA will allow us to impose tighter constrains on the physical properties of this rather interesting low-mass galaxy.